GRANT AGREEMENT No.: 764902 **Project Acronym: TOMOCON** **Project title: Smart tomographic sensors for advanced industrial process control**	TOMOCON Smart Tomographic Sensors for Advanced Industrial Process Control
Deliverable Rel. No. **D2.4.**	Lead Beneficiary **UEF**
EU Del. No. **D8**	Type **Report**
WP No. **WP2**	Date: **25.03.2021** — Revision: **0**

Innovative Training Network

TOMOCON

Deliverable Title

Smart Tomographic Sensors and Implemented Real-time Data Processing for Demonstrations

Description

This deliverable is a summary report on the implemented tomographic sensors for the four industrial demonstration cases, including the physical principles, hardware implementation, data processing, implementation in process spaces and performance analyses.

Prepared by:	Prof. Dr. Marko Vauhkonen	Marko Vauhkonen
Approved by:	Prof. Dr. Uwe Hampel	U. Ha
Approved by Supervisory Board:		07.04.2021

Dissemination Level: **Public**

This project has received funding from the European Union's Horizon 2020 research and innovation programme under the Marie Skłodowska-Curie Grant Agreement No. 764902.

Revision Sheet

Revision Number	Purpose of Revision	Effective Date
0	Initial Issue	07.04.2021

This project has received funding from the European Union's Horizon 2020 research and innovation programme under the Marie Skłodowska-Curie Grant Agreement No. 764902.

Contents

This project has received funding from the European Union's Horizon 2020 research and innovation programme under the Marie Skłodowska-Curie Grant Agreement No. 764902.

This project has received funding from the European Union's Horizon 2020 research and innovation programme under the Marie Skłodowska-Curie Grant Agreement No. 764902.

1 Foreword

In this document, the implemented tomographic sensors of the TOMOCON demonstration cases are described. The report includes the description of the physical principles, hardware implementation, data processing, implementation in process spaces and performance analyses of the sensors. All demonstration cases and all sensor types are explained and analyzed. The document is structured such that the sensors are described under each of the four demonstration cases. The order of the descriptions is the following: inline fluid separation, microwave drying, continuous metal casting and batch crystallization.

This project has received funding from the European Union's Horizon 2020 research and innovation programme under the Marie Skłodowska-Curie Grant Agreement No. 764902.

2 Electrical resistance tomography in inline fluid separation

Inline Swirl Separators have been developed over the past decades as a compact and cheap alternative to separate the mixture [1]. Inside the devices, the mixture of different densities phases crosses a static swirl element and starts rotating. Due to centrifugal forces, the denser phase (water) is pushed against the pipe's wall and the less-dense phase (oil) is pushed towards the center of the pipe. The lighter phase accumulates in the center of the pipeline, creating a continuous core extracted by a pick-up tube placed at the end of the equipment [2]. Based on the flow properties upstream the separator, the light-phase core created by the static swirl element varies in size and eccentricity [3]. Electrical Resistance Tomography (ERT) is a promising non-intrusive measurement technique for real-time monitoring and parameter extractions of dynamic industrial processes [4]. When compared with the aforementioned modalities, ERT poses the advantages of non-hazardous, low implementation costs, high measurement speed, portability, and straight forward implementation [5]. The fundamental measurement protocol of ERT is to reconstruct the distribution of conductivity of the target medium based on electrical measurements of its boundaries. If the light-phase core and heavy-phase annulus present different conductivities (as in the case of oil-water), the distribution of conductivity is directly connected to the distribution of the fluids inside the separator. In industrial applications, current-voltage (CV-ERT) and voltage-current (VC-ERT) ERT instruments are being used. In CV-ERT instruments, the current is injected through an electrode, and the resulting voltage is measured, but the major drawback in this type of instrument is the spreading of the sensing field into the axial direction, i.e., the fringe effect, which results in the unreliable measurements and distorted reconstructed images. Whereas in VC-ERT instruments voltage is injected and current is measured such that one electrode is used as excitation electrode (source electrode) and the rest of the electrodes (sink electrodes). VC type of systems are able to work with a wider range of conductivities and are simpler than CV-ERT systems [6]. Both speed and spatial resolution are fundamental to monitor the separation of the fluids inside the Inline Swirl Separator in real time. Previous works based on the correction of the light-phase core size measured by the sensor via calibration against a camera were successful in increasing the accuracy of the ERT system for non-iterative schemes [7][8], partially fulfilling both requirements. Although the previous studies could improve the technique in the context of the application, there is an interest in pushing the limits of the spatial and temporal resolution of the system even further. A new data processing approach based on the physical concepts behind the ERT measurements, successfully applying them to characterize the light phase core from the minimal number of measurements possible and directly from the measured data without the reconstruction step, is being developed. This allows the device to acquire data faster, since less measurements are required, and instantaneously process it by simple and logical calculations.

2.1 ERT sensor design

2.1.1 ERT sensor and measurement electronics

A typical ERT measurement system consists of metal electrodes mounted across the periphery of the sensing area called the sensor, data acquisition electronics (DAE), and software for data storing and visualizations, as shown in Figure 1a. The VC-ERT Flow Watch from Rocsole Ltd, currently off the shelve, was used in these experiments. The system is connected to 16 stainless steel electrodes, placed in a single plane embracing the 90 mm outer diameter-81.4 mm inner diameter PVC pipeline. The electrodes are screws of 12 mm head and 5 mm thread size and are installed with a pitch of 5.1 mm. The electrodes are installed in

This project has received funding from the European Union's Horizon 2020 research and innovation programme under the Marie Skłodowska-Curie Grant Agreement No. 764902.

the pipelines via drilled holes and sealed using rubber sealing of 2 mm thickness installed in the inner side of the pipeline. A metal shield of 200 mm was installed around the sensor in order to reduce the effects of external electromagnetic disturbances in the measurements. This is particularly seen in Figure 1b showing the ERT sensor installed on the demonstration flow loop at TU Delft. Inhouse developed software TomoKis studio [9] was used for live image reconstruction and data acquisition. All the 256 measurements of each frame are saved by the sensor, at a frequency of 12 Hz. In order to match the impedance range of the signal with the target media, the electrodes were connected to the electronics using a signal conditioning unit. Coaxial cables type RG178 of length 2.5 m were used for the connection between measurement electronics and the sensor.

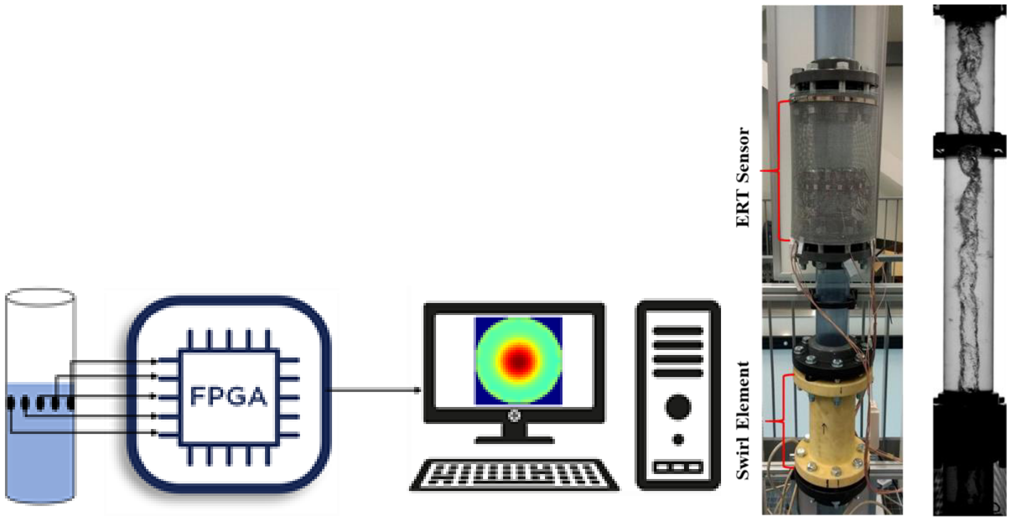

(a) (b)

Figure 1: (a) Structure of typical ERT system showing from left to right*: ERT based sensor, Data acquisition electronics, image reconstruction and visualization software. (b) Sensor installed on the TU Delft flow facility with corresponding camera view during liquid-gas separation.*

2.1.2 Sensor calibration

Six cylindrical 3D printed ABS phantoms are available for the static measurements, with diameters of 10 mm, 20 mm, 30 mm, 40 mm, 50 mm and 60 mm. The oil core of the original application (or air core of the dynamic tests) is expected to be more or less circular, being well mimicked by the insulating phantoms. The phantoms are placed at different positions inside the pipeline to mimic eccentric light-phase cores in the separator. Each phantom is measured in the center of the domain and in 8 eccentric positions towards different electrodes. To keep track of the center of the phantom, the distance from electrodes 1, 5, 9 and 13 was measured in millimeters (mm) using a ruler. The approach is illustrated in Figure 2, where Figure 2a shows the phantom of 20 mm placed in the center of the sensor and Figure 2b shows the four distances measured from the electrodes (L1, L2, L3 and L4).
The centroid of the phantom is recovered from the ruler measurements considering a Cartesian coordinate system with origin in the center of the domain, and solving the following least squares problem:

$$F(x_c, y_c) = \begin{cases} x_c^2 + (R - y_c)^2 - L_1^2 \\ (R - x_c)^2 + y_c^2 - L_2^2 \\ x_c^2 + (R + y_c)^2 - L_3^2 \\ (R + x_c)^2 + y_c^2 - L_4^2 \end{cases} \tag{1}$$

This project has received funding from the European Union's Horizon 2020 research and innovation programme under the Marie Skłodowska-Curie Grant Agreement No. 764902.

where the x_c and y_c are the centroid coordinates of the phantom obtained minimizing F. Although two measurements would be enough to track the phantom, an overdetermined system with four measurements was considered to reduce human errors when measuring the phantom position.

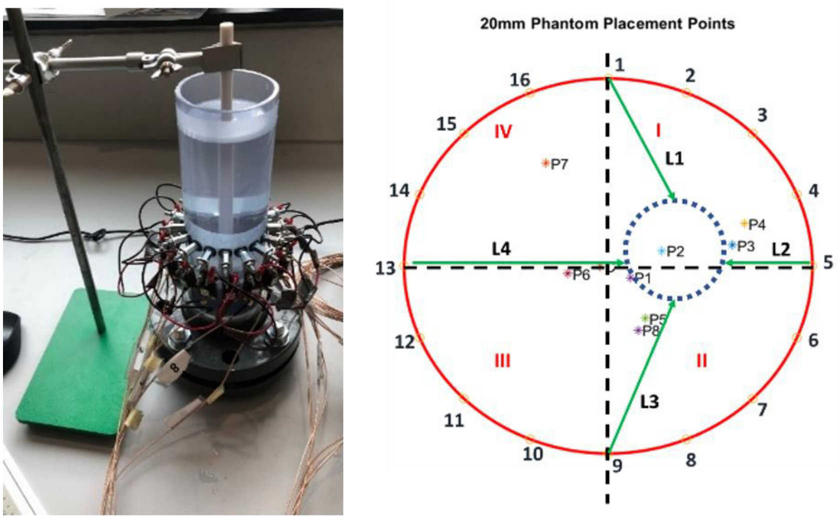

(a) **(b)**

Figure 2: (a) Placement of 20 mm phantom inside the physical sensor. (b) Distance measurement from positions L1, L2, L3 and L4.

2.1.3 Data processing algorithm

2.1.3.1 Core size

Due to the connection between the current value and the phantom size expected from the physics, the average of the 8 $\Delta i'$ values obtained by opposite measurements were plotted against the phantom diameter for each water conductivity considered. It was observed that the points collapse into the same curve, well described by:

$$D = -78.587\overline{\Delta\iota'}^2 + 135.3\overline{\Delta\iota'} + 4.333\ (R^2 = 0.98) \tag{2}$$

Where D is the diameter of the phantom and $\overline{\Delta\iota'}$ is the mean normalized current difference ($\overline{\Delta\iota'} = 0.125\sum_1^8 \Delta i'(k)$). The plot obtained is presented in Figure 3.

Dissemination Level: **Public**

This project has received funding from the European Union's Horizon 2020 research and innovation programme under the Marie Skłodowska-Curie Grant Agreement No. 764902.

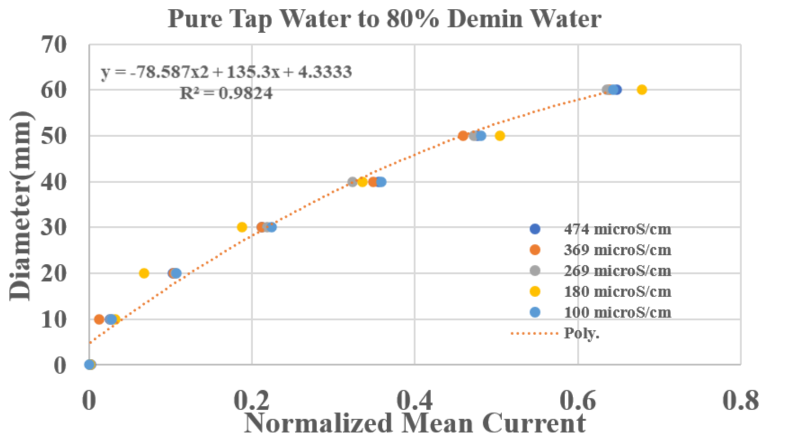

Figure 3: Plot of the diameter of phantom against the mean normalized current difference for different water conductivities. The blue dashed line represents the polynomial fit adopted to represent the relation.

2.1.3.2 Radial position

It was confirmed that the standard deviation between the eight opposite measurements was negligible when the phantom was in the centre of the sensing area and increased as the phantom was placed away from the centre. By plotting the position of the phantom against the standard deviation of current difference for all the experiments performed, the points collapse around a curve well approximated by

$$r = 6.333 \ln(std(\Delta i')) + 17.744 \ (R^2 = 0.92) \tag{3}$$

Where *r* is the radial position of the phantom. The curve and the original dataset are presented in Figure 4.

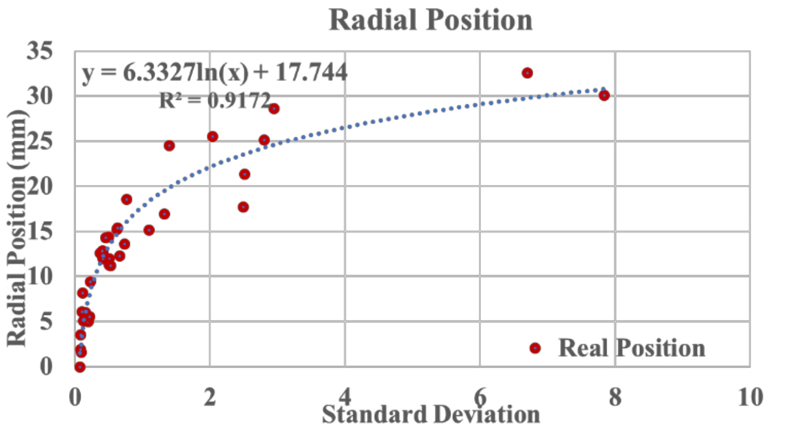

Figure 4: Fit obtained by plotting the change in normalized STD values against the radial position of the phantoms placed at different locations inside the domain. The blue dashed line represents the fit.

2.1.3.3 Angular position

Since the most distorted electric field line is obtained for the electrode pair aligned with the phantom, the smallest current observed indicates the line in which the phantom is located, between the electrode pairs used in the measurement. Additional measurements are required to define in which side of the electrode line the phantom is present. This is done by

This project has received funding from the European Union's Horizon 2020 research and innovation programme under the Marie Skłodowska-Curie Grant Agreement No. 764902.

four measurements of the current in 90 degrees turns, which divides the sensing area into four quadrants. Quadrants are defined between electrodes 1 and 5 (I), 5 and 9 (II), 9 and 13 (III) and 13 and 1 (IV). The presence of the phantom is either of these quadrants was also detected by the biggest deviation in the measured current, and the quadrant information is used to filter the three most affected $\Delta i'$. The approach of considering the three most affected currents instead of just the lowest one was motivated by the fact that sometimes the difference between the obtained values is small, and a mismatch between the quadrant and the electrode was observed (for instance, the quadrant obtained was 2, but the opposite measurements only cross quadrants III and IV). The measurements are made between electrodes of k and k+8, where k corresponds to the electrode pair (1 to 8). If the quadrants I or II are observed, the most affected electrode is in the range 1 to 8, and if the quadrants III or IV are observed, the electrode is in the range 9 to 16. Once the electrode is obtained from the combination between the line information and the quadrant, the angle in relation to electrode 1 in the clockwise direction is calculated by multiplying the electrode number by the distance between electrodes, leading to $\theta = (\text{k-1})\ 22.5^{\text{o}}$ if the quadrant is I or II and $\theta = (k+7)\ 22.5^{o}$ if the quadrant is III or IV. The complete algorithm is summarized in the flow chart of Figure 5.

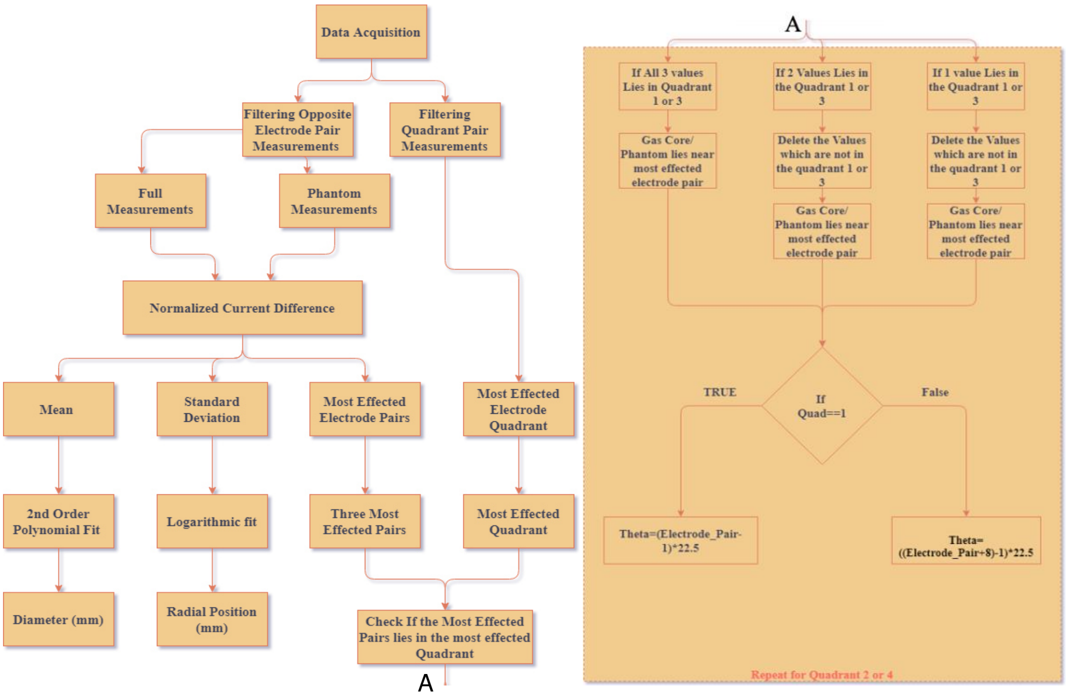

Figure 5: Algorithm flow chart showing all the steps needed to extract the geometrical parameters from raw ERT data.

2.1.4 Static and dynamic experimental results

Figure 6 presents the reconstructed size and position of the insulating region obtained by the algorithm for the slightly off-center point P2 for all the phantoms, plotted together with the real position and size of the elements. A good overlap between the real and predicted geometry is obtained by the technique.

This project has received funding from the European Union's Horizon 2020 research and innovation programme under the Marie Skłodowska-Curie Grant Agreement No. 764902.

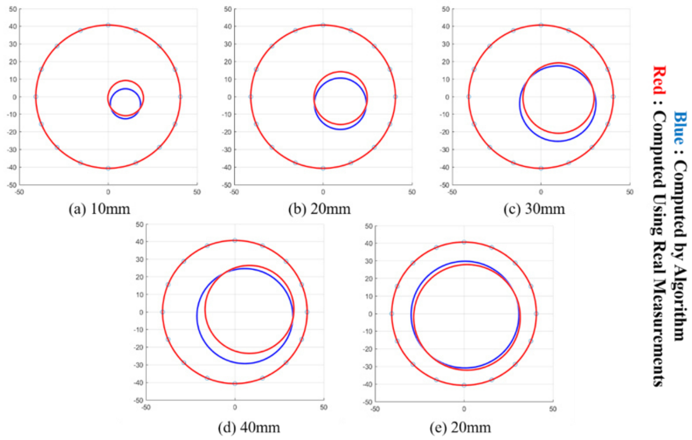

Figure 6: Comparison between the algorithm reconstruction (blue) and the real phantom characteristics (red) for the point P2 and phantom sizes between 20mm and 60mm.

The algorithm results were also compared with the tomograms, that would originally provide the same quantities in a real scenario. A low spatial-temporal resolution was chosen as reference, due to the requirement of fast processing schemes for the real time monitoring of the separation. From the applied context, measurements with the core close to the center of the domain are the most important for the process. Figure 7 shows the comparison of proposed technique (blue circles) with the tomograms obtained using the Gauss-Newton image reconstruction scheme. The figure shows that the visualizations obtained from the algorithm strongly correlate with the tomograms in terms of positions, but a considerable difference in the diameter estimation is present. In past studies [30], the image reconstructions overestimate the diameter by 98 % in the smaller sizes of the phantom and gradually improve with the larger phantoms.

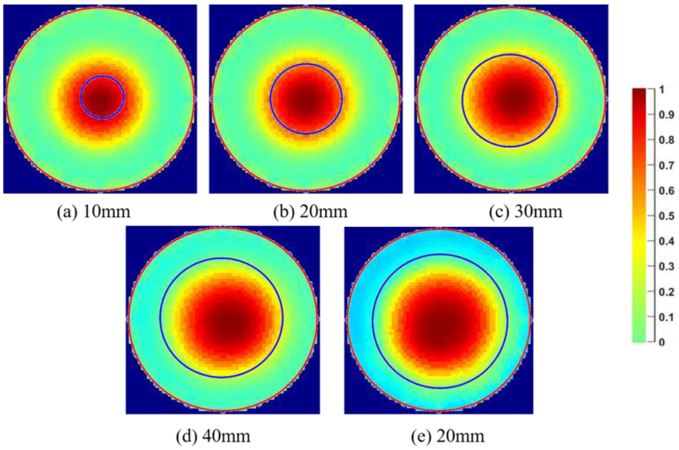

Figure 7: Diameter and position obtained using algorithm superimposed on the traditional tomograms at the central positions. Case 20 mm to 60 mm.

The comparison between the core size obtained by the camera and by the proposed ERT algorithm is presented in Figure 8. It shows that the behavior captured during inline measurement of the liquid-gas separation on the TU Delft flow facility previously presented in Figure 1b by the camera is well represented by the ERT, with a cross correlation factor of 0.93. In terms of average, both signals present similar values: 22.8 mm for the camera and 21.7 mm for the ERT.

This project has received funding from the European Union's Horizon 2020 research and innovation programme under the Marie Skłodowska-Curie Grant Agreement No. 764902.

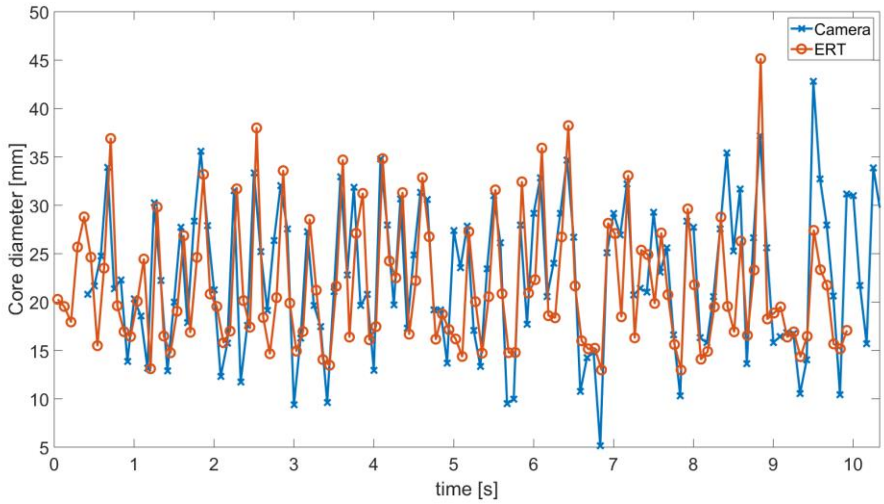

Figure 8: Time series comparison of the diameter between ERT and camera at the point of maximum cross-correlation between the signals.

When comparing the temporal resolution, the tomograms required 98.6 s to reconstruct 2 minutes of data (1800 frames) using Intel Core i7 CPU and 16.0 GB RAM, whereas the algorithm can compute all the parameters in 0.12 s, 0.12 % the original time. The first attempt of real time gas core monitoring done on the flow facility at TU Delft was validated by continuously sending the geometrical parameters computed from the proposed algorithm to a LabVIEW code via a dynamic link library (DLL). The DLL connects the Tomokis Studio, filters the raw data, and computes the radial position, diameter, and azimuthal position based on the equations described.

2.2 Conclusion

A data reduction technique was adapted, and only 12 measurements out of 256 were considered to obtain the geometrical parameters. First, the phantoms of known diameter were placed at nine different positions, and the real positions were measured using rulers. Based on the eight opposite electrode pair measurements, mathematical models were formulated to estimate the diameter and the radial position of the phantom. A careful quadrant-based method was devised to retrieve the azimuthal angle by considering four additional measurements. The parameters retrieved using the proposed algorithm were first compared with the ruler measurements, and later with the image reconstructions. Both comparisons have shown a good agreement between each other. Due to the ability to process the raw data, the proposed algorithm computed the parameters 99.87 % faster than using the tomograms, which allows a proper real time monitoring of the separator. To summarize, the proposed algorithm successfully qualifies the electrical resistance tomography data processing technique for real-time monitoring of swirling two-phase flows.

2.3 References for ERT in IFS

[1] B. Sahovic *et al.*, Controlled Inline Fluid Separation Based on Smart Process Tomography Sensors, *Chemie-Ingenieur-Technik*, Vol. 92, No. 5, pp. 554–563, 2020.

[2] B. Sahovic, H. Atmani, P. Wiedemann, E. Schleicher, D. Legendre, E. Climent, Investigation of upstream and downstream flow conditions in a swirling inline fluid separator – experiments with a wire-mesh sensor and CFD studies, *9th World*

This project has received funding from the European Union's Horizon 2020 research and innovation programme under the Marie Skłodowska-Curie Grant Agreement No. 764902.

Congress on Industrial Process Tomography, pp. 1–10, 2018.

[3] M. A. Sattar *et al.*, Multichannel Capacitive Imaging of Gas Vortex in Swirling Two-Phase Flows Using Parametric Reconstruction, *IEEE Access*, Vol. 8, pp. 69557–69565, 2020.

[4] S. Liu, J. Jia, Y. D. Zhang, Y. Yang, Image Reconstruction in Electrical Impedance Tomography Based on Structure-Aware Sparse Bayesian Learning, *IEEE Trans. Med. Imaging*, Vol. 37, Vo. 9, pp. 2090–2102, 2018.

[5] Z. Ren, A. Kowalski, T. L. Rodgers, Measuring inline velocity profile of shampoo by electrical resistance tomography (ERT), *Flow Meas. Instrum.*, Vol. 58, pp. 31–37, March 2017.

[6] M. A. R. Frias and W. Yang, Electrical resistance tomography with voltage excitation, *Conf. Rec. - IEEE Instrum. Meas. Technol. Conf.*, Vol. 2016, No. 1, pp. 1–6, July 2016.

[7] M. A. Sattar, M. M. Garcia, R. Banasiak, L. M. Portela, L. Babout, Electrical Resistance Tomography for Control Applications: Quantitative Study of the Gas-Liquid Distribution inside A Cyclone, *MDPi Sensors*, Vol. 20, No. 21, p. 6069, 2020.

[8] G. Rao, M. A. Sattar, L. Jackowska-Strumiłło, Quantitative evaluations with 2D Electrical Resistance Tomography in the low conductivity solutions using 3D printed phantoms for crystallization process monitoring, *Sensors*, Vol. 21, No. 2, p. 564, 2020.

[9] R. Banasiak, R. Wajman, T. Jaworski, P. Fiderek, P. Kapusta, D. Sankowski, Two-Phase Flow Regime Three-Dimensonal Visualization Using Electrical Capacitance Tomography – Algorithms and Software, *Informatics Control Meas. Econ. Environ. Prot.*, Vol. 7, No. 1, pp. 11–16, 2017.

This project has received funding from the European Union's Horizon 2020 research and innovation programme under the Marie Skłodowska-Curie Grant Agreement No. 764902.

3 Introduction to WMS in inline fluid separation

The wire-mesh sensor (WMS) is a special type of tomographic sensor capable of acquiring cross sectional phase fraction information at a significant higher rate compared to other conventional tomographic sensors.
Due to its high temporal and also high spatial resolution, the wire-mesh sensor is an ideal candidate to measure fluid mixture composition at a high volumetric flow rate. A reasonably fast computational processing system is required to handle acquisition, analysis, calculation, processing and transfer of results in form of gas/water fraction and mixture flow velocity. For this purpose, a new hybrid computational system is being developed to enable the use of a wire-mesh sensor as an inline process measuring device. Fluid separation is a typical task in many fluids processing applications typically found in the oil and gas industry.
The basic principle of the inline fluid separation process is the creation of a lesser dense phase in the middle in form of vortex pushing the denser phase to the wall.
Inline fluid separation uses centrifugal force with much higher strength than gravitational force which causes the separation.
The centered fluid is extracted via a pick-up tube. Following the direction of the flow, the wire-mesh sensor is placed upfront of the swirl element (Figure 9). The decision of the sensor placement is decided by analyzing the results obtained from experimental observation and empirical calculation. The outcome of previously mentioned actions has shown that the sensor is capable of predicting the gas core diameter downstream within an error of +/- 10 % [1].

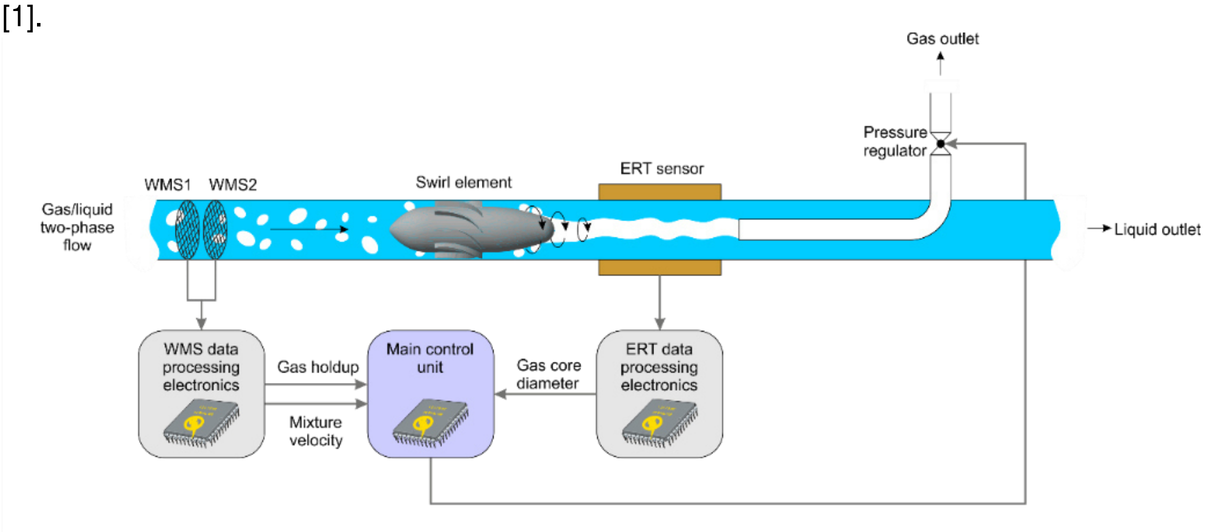

Figure 9: Principle of tomography-controlled inline fluid separation, here for water-air separation.

An exemplary system with a pair of adjacent wire-mesh sensors is shown in Figure 9. The second sensor is needed for mixture velocity calculation explained later in this report.
A pick-up tube placed inside the pipe in the downstream section extracts the lesser dense fluid from the centered rotating core. Imaging or other sensors are placed upstream and downstream of the swirl. Such sensors can be e.g. electrical tomography sensors [2], wire-mesh sensors [3] or simpler sensors, like ultrasound sensors or optical probes. Instability and temporal fluctuation of the core are characterized by a change in diameter and waviness, that is, fluctuation around the mean diameter and the standard deviation from the average core diameter. An ideal core may be one that has a geometry close to an ideal cylinder with

This project has received funding from the European Union's Horizon 2020 research and innovation programme under the Marie Skłodowska-Curie Grant Agreement No. 764902.

a diameter equal to the one of the pick-up tube. Then, the separation efficiency would be continuously optimal.

3.1 Wire-mesh sensor

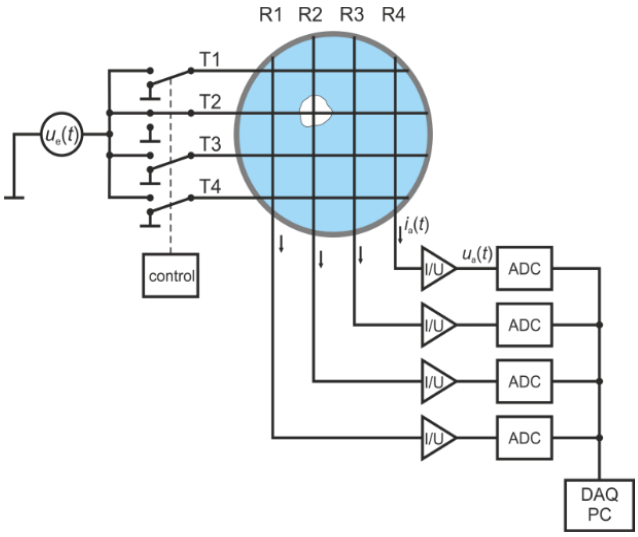

Figure 10: Schematics of a conductivity wire-mesh sensor.

For upstream data acquisition and processing, we used a conductivity wire-mesh sensor (Figure 10). A wire-mesh sensor consists of two planes of parallel wires in the pipe cross-section. The wires are made of stainless steel.
The two planes are separated by a small axial distance and arranged so that they form an angle of 90° to each other. In the transmitter plane, wires are sequentially activated with a square wave excitation voltage signal while at the receiver wires in the other plane transmitted electrical currents are simultaneously sampled. This way the electrical conductance in the crossing-points is obtained with a high speed of up to 10,000 frames per second. In our experiments the wire-mesh sensor works on the principle of measuring electrical conductivity of the passing fluid. The wire-mesh sensor in our experiments is made of a 16x16 electrode grid. Spatial and axial resolution are 3.125 mm and axial 1 mm, respectively. Information contained in the current produced from the crossing points of the transmitter and receiver wires is transformed into voltage signal by a transimpedance amplifier stage. Voltage signals are sampled by analog-to-digital converters (ADC). Digitized signals are further processed on a workstation type computer.

3.1.1 WMS void fraction analysis

In order to calculate the local instantaneous void fraction values $\varepsilon_{i.j.n}$ of a crossing with indices i, j and the frame number n from the measured signals $U_{i,j,n}^{meas}$, usually a first order approximation is used. The Maxwell or parallel relation between measured signal and the local gas holdup within the corresponding area of the virtual wire crossing is used:

$$\varepsilon_{i.j.n} = \frac{1-g_{i,j,n}}{1+\frac{1}{2}\cdot g_{i,j,n}}, \; g_{i,j,n} = \frac{U_{i,j,n}^{meas}}{U_{i,j}^{W}} \tag{4}$$

Dissemination Level: **Public**

This project has received funding from the European Union's Horizon 2020 research and innovation programme under the Marie Skłodowska-Curie Grant Agreement No. 764902.

Here, $U_{i,j}^{W}$ denotes the local signal for a water only measurement, which is usually the time averaged sensor signal of the full water calibration measurement. The averaged void fraction is then calculated as

$$\overline{\varepsilon_n} = \sum_i \sum_j a_{i,j} \cdot \varepsilon_{i,j,n} \ , \ \bar{\varepsilon} = \frac{1}{N} \cdot \sum_{n=1}^{N} \overline{\varepsilon_n}. \tag{5}$$

with $\varepsilon_{i,j,n}$ denoting the measured void fraction in the crossing point i, j. The variable $a_{i,j}$ is a weight coefficient that denotes the share of a crossing point with the cross-section and $\bar{\varepsilon}$ is the average void fraction across the spatial and temporal domain.

As mentioned above, the calibration file, used to calculate instantaneous void fractions having mesh point values $U_{i,j}^{W}$, is usually obtained by averaging those values in a gas free flow with only water flowing through the pipe. The downsize of this calibration method is to have conductance values of mesh points in a pure water flow taken before the actual measurement. This leads to an inaccurate voltage signal representation of pure water flow due to changes in conductance or temperature values that might occur over time e. g. due to heat up by the pump in a closed uncooled loop. Thus, another calibration method is using the pointwise histogram of one entire measurement. The histogram shows the frequency of different conductivity occurrences formed as an array. The value for the calibration file is the bin position of the highest value in the second part of the array with bin values indicating conductivity values of full water. In our case the histogram is created with bin numbers equal to the highest value a single spatial point can have, which is 4096.

From the histogram it is clear that there can also be slightly higher values than the peak value. Appearance of higher conductance values is caused by temporary increase in the electrical potential field around a mesh point in an air and water mixture flow. One case of such behaviour is registered by mesh points which are on the border and nearby of passing bubbles [3]. The second case are higher measured conductance values in the bulk fluid in case of stratification or larger plug bubbles. This effect can be explained by non-ideal electronics circuit conditions. An ideal trans-impedance amplifier has a resistance of zero on its negative input. However, since the wires always have a small axial resistance this value is not ideally zero. Even if deionized water has a low conductivity, this wire resistance leads to a voltage divider and a small portion of current flows towards the grounded transmitter wires instead towards the amplifier input. Thus, the measured signal in a completely liquid filled pipe is smaller than e. g. in a pipe with 25 % water at the bottom for the same crossing.

Therefore, receiver wires may also measure higher conductance of a mesh point being fully occupied by water, in mixture of air water flow, compared to the same mesh point condition in a pure water flow, even in regions far from the gas liquid interface. This effect is stronger for long and thin wires, small grid spacing and higher liquid conductivity values.

It was shown that the linear method overestimates the averaged void fractions, especially in case of bubble flows. The analyses in [4] were based on the Maxwell method for the calculation of the local instantaneous void fraction and have shown that a higher accuracy in the average void fraction calculation was obtained in comparison to the linear relationship between the void fraction and the measured signal. The method does not cut off negative void fractions.

Negative values are kept only if they occur at the liquid gas interface. Negative values in the bulk region are set to zero otherwise the algorithm has derived negative results for the cross-sectional averaged void fraction for particular cases. In contrast to equation (5), the cross-sectional averaged void fraction is thus obtained through

This project has received funding from the European Union's Horizon 2020 research and innovation programme under the Marie Skłodowska-Curie Grant Agreement No. 764902.

$$\overline{\varepsilon_n} = \sum_i \sum_j a_{i,j} \cdot b_{i,j,n} \cdot \varepsilon_{i,j,n} \tag{6}$$

where $b_{i,j,n}$ are the elements of the bulk removal mask. A sequence of specified actions leading to an efficient removal of unwanted signals with its detailed description can be found in [1].

3.2 Hybrid computational system for WMS data processing

3.2.1 Tomocon electronics

The Tomocon electronics has been developed in collaboration with Teletronic Rossendorf GmbH and the name is given after the Tomocon project. Its main functionality is to forward packed raw wire-mesh sensor data to the data acquisition card via VHDCL (Very high-density cable connect) protocol. A depiction of connections, signal characteristics, clock rates and parts of the electronics can be seen in Figure 11. The electronics is split into two main functional boards. A custom-made driver board and an Arty S7 board which features the Xilinx Spartan-7 FPGA. The driver board regulates the current and controls the signal between the Arty S7 board and the transmitter/receiver modules attached to the wire-mesh sensor. The transmitter and receiver module perform analog-to-digital and digital-to-analog conversion respectively. The role of the FPGA board is to generate input signal for the transmitter module and forwarding the signal. The signals obtained from the receiver wires are being multiplexed and transferred at a bit rate of 10.24 MB/s over a VHDCL cable to the data acquisition board. The signal transmitter frequency is 1.33 MHz and the receiver is clocked at 40 MHz.

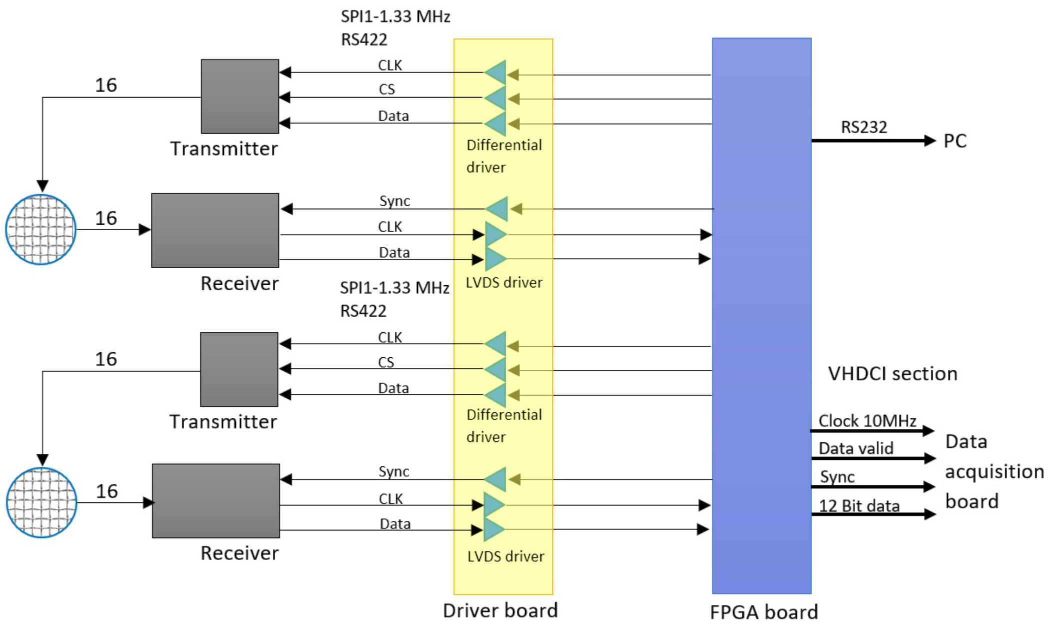

Figure 11: Simplified diagram of the Tomocon electronics with components and signal characterization information.

This project has received funding from the European Union's Horizon 2020 research and innovation programme under the Marie Skłodowska-Curie Grant Agreement No. 764902.

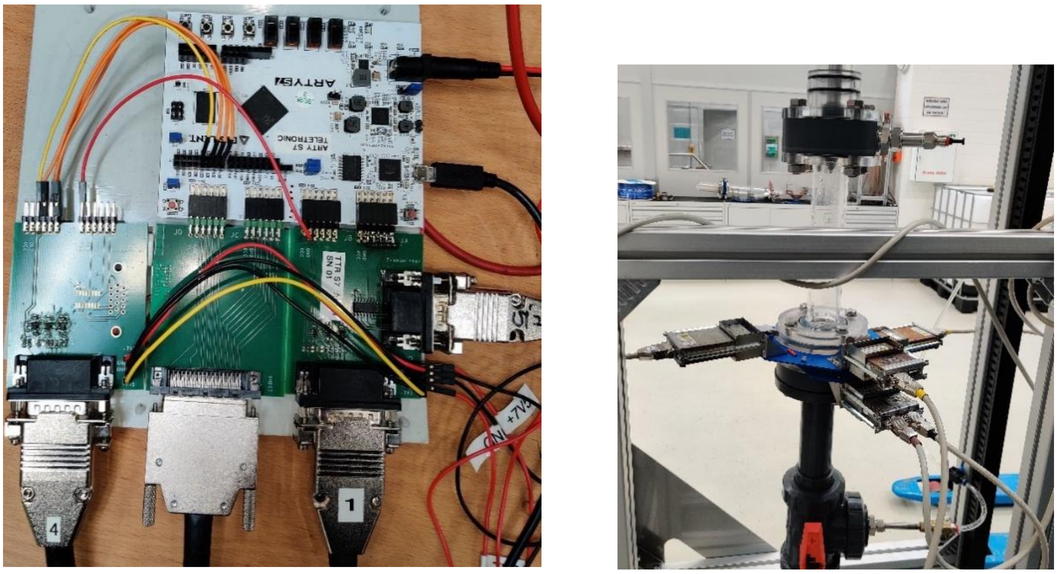

Figure 12: High-resolution photo of the Tomocon board v2.0 (left), double wire-mesh sensor integrated into the flow setup at HZDR TOPLOW+ facility.

Figure 13: Data acquisition card and graphic card mounted to the motherboard.

This project has received funding from the European Union's Horizon 2020 research and innovation programme under the Marie Skłodowska-Curie Grant Agreement No. 764902.

3.3 Workstation hardware specification and software implementation

The two other processing units, the GPU (graphic processing unit) and the CPU (central processing unit), are part of the workstation. As the raw data is forwarded from the Tomocon board, the task of the GPU and CPU is to process the data and output void fraction and area velocity of the multiphase flow. The CPU is an Intel® Core™ i9-9900K Processor and the GPU a NVIDIA® Quadro RTX™ 5000 (Figure 13). Due to the functional capability of the graphic card to perform highly efficient computation on algorithms designed to work on the principle of SIMT (single instruction and multiple threads) and SIMD (single instruction multiple data), the algorithms were constantly modified to fully use the processing power of the GPU.
Data from the Tomocon board is temporarily stored in the allocated buffer on the data acquisition cards dedicated memory. The type of card is an M4i.77xx-x8 series digital waveform acquisition card from Spectrum Instrumentation GmbH. With its 32 single ended synchronous channels, the number of channels is sufficient to receive dual WMS raw data which requires only 12 single-ended ones. Theoretically, the data acquisition device is capable of connecting two Tomocon boards and up to four wire-mesh sensors having WMS with 16x16 wire configuration. The problem is the clock signal synchronization for the Tomocon boards. An advantage of the data acquisition card compared to standard devices is the full programmability of its features which can be written in C++. This useful option could allow us to sync the signals from the boards via the internal clock of the card and use the external trigger for recording. Further investigation will be done.
For this card two modes of operation are useful for us: The FIFO (first in, first out) and the ring buffer mode. Each mode is used in a different matter. The FIFO mode is used for a continuous data transfer between the acquisition card and the PC's main memory or hard drive storage. In the ring mode, the data is stored on the card memory and transferred to the RAM memory when a trigger is detected. Due to our raw wire-mesh data size and the rate at which it is forwarded, the FIFO mode is a better choice. Local benchmarks from the card's manufacturer are also showing faster data transfer in FIFO mode. The ring mode is ideal for larger data packages like larger and more detailed cross-sectional images of tomographic sensors or multiple sets of sensors. Online measurement with acquisition rate will use the ring mode to calculate flow parameters in larger time acquisition.
Initial algorithm development was done in MATLAB and later finalized in C++ and CUDA. The integrated development environment used for this application is Microsoft Visual Studio 2019.
NVIDIA® Nsight™ Compute is used for profiling CUDA code by estimating its performance via extracted relevant metrices like achieved occupancy, atomic transactions, branch efficiency etc.

3.4 Data handling and processing

The final application is an executional file extracted from VS 2019 environment. The recording of incoming data samples is done by the acquisition card driver which adjacently places one sample after another onto an allocated space in the RAM memory. Transferring data from the card to the PC's RAM is accomplished by DMA (direct memory access). Reading the data from the buffer happens after 500 iterations of sample writing. Each sample is a set of conductivity values representing the cross-sectional area captured by the wire-mesh sensor.
The array is demultiplexed by applying binary shift operations and the results are copied to a two-dimensional array having 12+1 rows/channel. The first 12 are containing the original 12-

This project has received funding from the European Union's Horizon 2020 research and innovation programme under the Marie Skłodowska-Curie Grant Agreement No. 764902.

bit raw sensor information while the last one is the validation signal used for jitter removal. Wire-mesh sensor frames are created from these channels (Figure 14b). Afterwards the histogram is calculated for each cross-sectional point. The histogram uses 50K frames for creating a calibration frame (Figure 14c). This process is repeated continuously through the entire measurement.
The final stage is the removal of negative void fractions in bulk areas (water concentrated) and the calculation of the average void fraction for 500 frames.

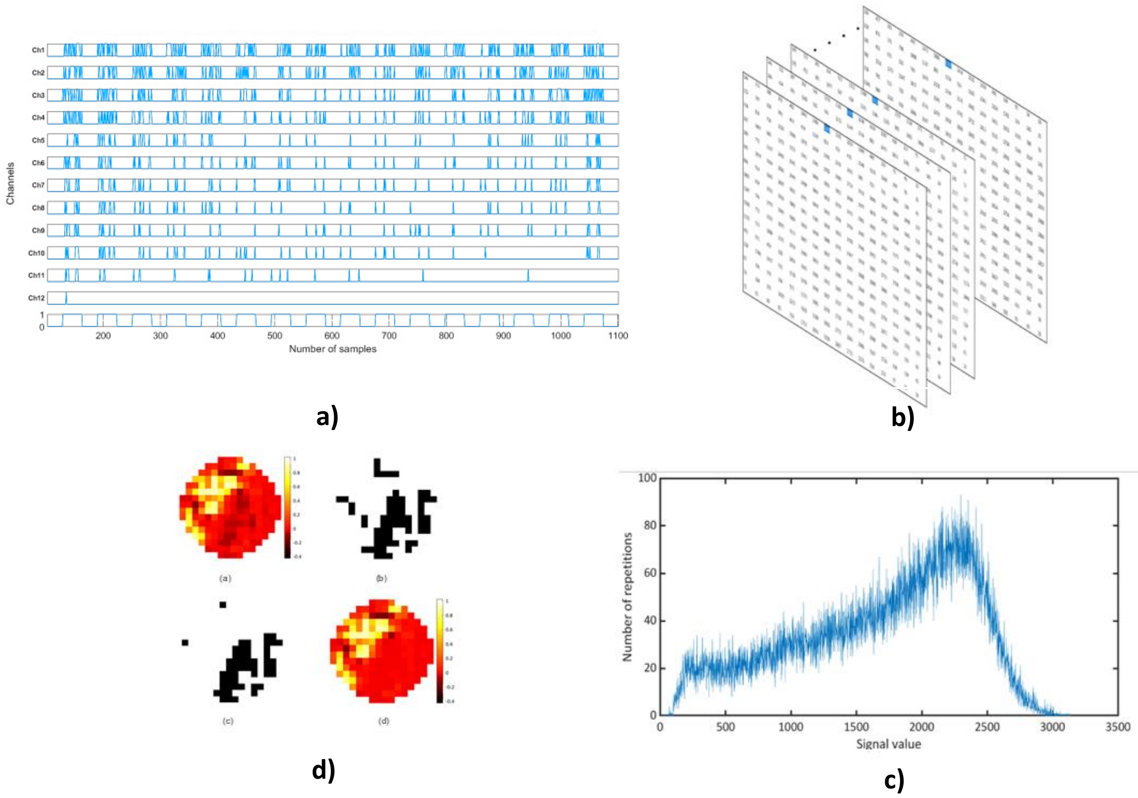

Figure 14: Graphical code illustration for void fraction application a) Raw wire-mesh signal data 12-bit format, b) Cross-sectional conductance values, c) Histogram of one spatial point, d) Procedure of negative void fraction removal.

3.5 Algorithms and computational stability

Computationally more demanding calculations were done asynchronously on the GPU without the main processor being on hold. Each CUDA capable device uses its many processing cores to perform concurrent calculation. Kernel (function executed by the GPU) execution is represented in form of threads which are the smallest performed operation of the kernel controllable by the user. Each algorithm has been optimized to a certain degree, but penalty in form of execution time still occurs due to warp divergence, global memory usage instead of shared, global memory access restriction, bank conflict etc. Each algorithm is complex in design and the throughput can be even higher. In our case further optimization of the code is unnecessary because the desired transferred rate is achieved.
Pinned memory is used for host (reserved to be used by the CPU) memory allocation. The number of points in each frame is 256, which is also the number of threads in each block. All

This project has received funding from the European Union's Horizon 2020 research and innovation programme under the Marie Skłodowska-Curie Grant Agreement No. 764902.

of the matrices have been written in one dimensional form which is the form in which they are being stored in memory. Each thread value is the index number in a frame.
These algorithms are part of an upcoming paper and will not be explained in much detail. Here, the void fraction calculation is using constant memory for calibration and geo files (containing weight coefficients of eq. 4). Variables allocated to the constant memory do not restrict simultaneous access to its values which allows threads from each block to access the constant memory at the same time and achieve concurrency.
The main performance gain is estimated by measuring its execution time using high resolution clock function (HRC). Our first major test was a comparison of just the void fraction data transfer via UDP transfer. For 10 seconds of data recording, the HRC measures 10.27 seconds which consist of 10 seconds of two WMS recordings (2x10x10K frames) and 0.27 seconds of raw data transfer, computational calculation and the complete transfer of the results via UDP to a control unit using GPU+CPU. The HRC for the CPU is 12.7 seconds. With the introduction of the histogram into the application, the CPU needed 3 seconds additionally to perform the histogram calculation. Further comparison will not be done as the CPU computational power alone cannot keep up with the combination of the CPU+GPU performance.

The velocity of the incoming mixture flow is calculated by dividing the physical distance between two wire-mesh sensors and the lag determined by cross correlating the two wire-mesh sensor signals. Each point in a frame has its own calculated mixture flow velocity. The method does work well for measurements being acquired for several seconds. The lowest measurement time for obtaining a stable signal correlation is 2 seconds. Below this time frame instabilities are occurring as NaN (nan available number-division by zero) values and numerically distant values between neighboring spatial points.
To increase the peak estimation two approaches are being investigated. One is the addition of Gaussian white noise (GWN) to the instantaneous void fractions. The two signals with the GWN are statistically independent until they match in the correlation calculation and produce a distinguished peak from which the lag is determined.
Second is the quadratic and spline interpolation of spectral peaks which will give us a more precise estimate of the offset by increasing the bin (present signal frequencies) resolution.
Both approaches are producing good results is some cases. Unfortunately, instabilities are still happening. Further improvements to the methods are still needed.

3.6 Conclusion

The wire-mesh sensor connected to the hybrid system can be integrated into a fluid separator to send relevant process information to a control unit. Its rate of acquisition, processing time and transfer rate are delivered to the controller in less time than the time a physical value changes in the flow, which is considered to be an online measurement. At the moment the complete inline WMS system is able to fully acquire cross-sectional images from two WMS at a rate of 10 K and deliver an average void fraction from a set of 500 frames at a rate of 20 Hz. The velocity measurement at this state does not provide high reliability to be able to be used as a measurement value. However, the calculated velocity changes significantly when a slug passes through the wire-mesh sensor.
Additional statistical parameters of the flow using the void fraction calculation like variances, standard deviation and frequency oscillation around the mean can been integrated into the final code as they do not require high computational throughput.
With the addition of the mixture velocity, the system will be capable of calculating additional parameters relevant to the flow like superficial gas and liquid velocities.

This project has received funding from the European Union's Horizon 2020 research and innovation programme under the Marie Skłodowska-Curie Grant Agreement No. 764902.

Theoretically the computational power of the hybrid system is more than enough to have this additional calculation as a part of the final application.

3.7 References for WMS in IFS

1. B. Sahovic, H. Atmani, P. Wiedemann, E. Schleicher, D. Legendre, E. Climent, R. Zamanski, A. Pedrono, U. Hampel, A study on the relationship between upstream and downstream conditions in swirling two-phase flow, *Flow Measurement and Instrumentation*, Volume 74, 2020.
2. S.M. Huang, C.G. Xie, R. Thorn, D. Snowden, M.S. Beck, Design of sensor electronics for electrical capacitance tomography, *IEEE Processing*, 139 (1), 1992.
3. M. Da Silva, E. Schleicher, U. Hampel, Capacitance wire-mesh sensor for fast measurement of phase fraction distributions, *Meas. Sci. Technol.*, 18, 2007.
4. H.-M. Prasser, Signal response of wire-mesh sensor to an idealized bubbly flow, *Nucl. Eng. Des.*, 336, 2018.

This project has received funding from the European Union's Horizon 2020 research and innovation programme under the Marie Skłodowska-Curie Grant Agreement No. 764902.

4 Microwave drying

Drying of dielectric materials is one of the standard processes in several industries. Among different drying technologies, microwave drying is becoming an attractive candidate for drying high moisture materials. One of the main goals in this process is to achieve an as uniform moisture distribution inside the material as possible since it has a high impact on the final product quality. Typically, the aim is to reach a certain level of moisture in the dried material. Designing an advanced moisture controller for the microwave drying process can help to get a homogenous moisture distribution. However, moisture distribution information and a process model are required to derive this controller.

Our research aims to develop two different tomography sensors to measure the moisture distribution of polymer foams in a microwave drying process: Electrical capacitance tomography (ECT) sensor and microwave tomography (MWT) sensor. Figure 15 shows a picture of our testbed microwave system called HEPHAISTOS, located at Karlsruhe Institute of Technology (KIT), Karlsruhe, Germany. Both ECT and MWT reconstruct the 2D/3D permittivity distribution of the polymer foam, which correlates with the moisture content. The estimated moisture from ECT or MWT is then used as feedback to the moisture controller. The structure of the closed-loop control for the microwave drying demonstration is illustrated in Figure 16.

Figure 15: The HEPHAISTOS industrial drying system with conveyor-belt located at Karlsruhe Institute of Technology (KIT), Karlsruhe, Germany.

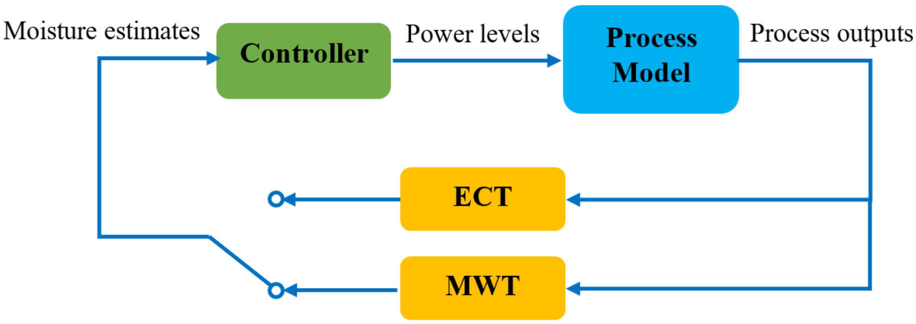

Figure 16: Microwave drying process closed-loop control.

This project has received funding from the European Union's Horizon 2020 research and innovation programme under the Marie Skłodowska-Curie Grant Agreement No. 764902.

5 Electrical capacitance tomography in microwave drying

Electrical capacitance tomography is an attractive tool for monitoring moisture distribution in several applications since it is non-intrusive, non-invasive, and inexpensive [1]–[3]. Our research aims to design an ECT sensor to estimate the moisture distribution of polymer foams in the microwave drying process, see Figure 15.

The ECT measures the contact-free capacitances between the electrodes mounted on a frame around the foam after the drying process. The measurements are then employed in a reconstruction algorithm to estimate the foam permittivity distribution. Since the material permittivity correlates with the material moisture, a calibration curve between the estimated permittivity and the actual moisture of the material is determined. The moisture distribution of the material can be recovered by employing the calibration curve on the estimated permittivity distribution. The moisture estimates can then be employed as feedback for the moisture controller unit, as shown in Figure 16. Figure 17 illustrates a schematic picture of the microwave system considered in this study while the designed ECT sensor is installed at the exit point. The next sections explain the theory behind ECT, its design and hardware, and the experimental results.

5.1 Theory

To solve the reconstruction problem in ECT, which is also referred to as the inverse problem, we need to solve the forward problem first. The forward problem formulates a model to connect the ECT measurements, the electric potential distribution, and the permittivity distribution. The forward model here is the complete electrode model derived for ECT [4].

The forward model is numerically solved using the finite element method [4]. By augmenting the models corresponding to a set of measurements in a vector and assuming additive measurement noise, the observation model for ECT can be formulated as

$$\mathbf{C} = \mathcal{H}(\boldsymbol{\epsilon}) + \boldsymbol{v}. \tag{7}$$

In model (7), $\boldsymbol{C}$ denotes the vector of the measured electrical capacitances between the electrodes, $\boldsymbol{\epsilon}$ is the discretized permittivity distribution, $\mathcal{H}$ is the map between the permittivity distribution, $\boldsymbol{\epsilon}$, and capacitances, $\mathbf{C}$, and $\boldsymbol{v}$ is the additive measurement noise.

This project has received funding from the European Union's Horizon 2020 research and innovation programme under the Marie Skłodowska-Curie Grant Agreement No. 764902.

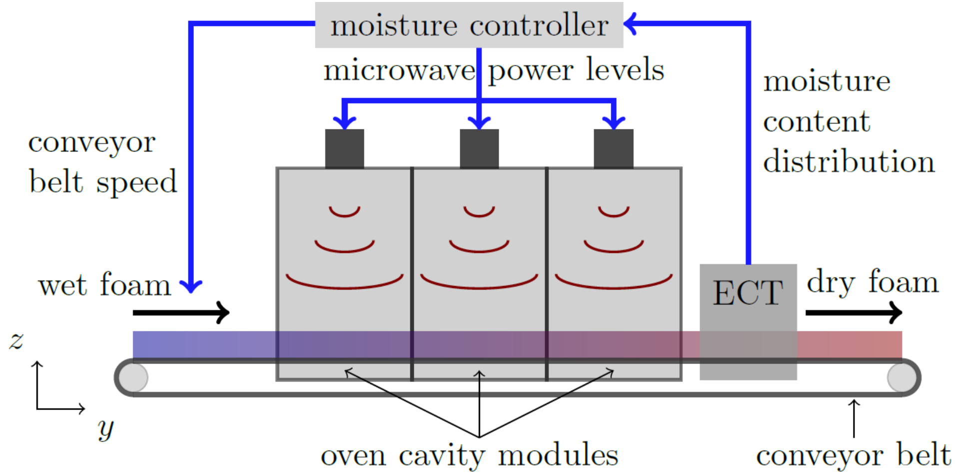

Figure 17: A schematic picture of the microwave drying system.

The observation model (7) connects the measured electrical capacitances with the permittivity distribution and is mathematically a well-posed problem. However, the inverse problem is an ill-posed problem aiming to reconstruct the permittivity distribution based on the capacitance measurements. In this research, the difference imaging method is employed to reconstruct the permittivity changes of the wet material compared to the permittivity of the dry material [4]. The chosen technique is a linear method; therefore, it is computationally fast and suitable for real-time measurements, which is necessary for having a closed-loop moisture controller for the microwave drying process. However, due to the approximation error of the linearization, there can be a relatively high estimation error for the permittivity change value when using the difference imaging method. A calibration curve between the estimated permittivity change calculated from the reconstruction algorithm and the actual moisture of the foam can be obtained to estimate the moisture distribution.

5.2 Design

Several factors in designing the ECT sensor can considerably affect the reconstruction accuracy and the sensor spatial resolution. Among these factors are the number of the electrodes, the electrode size, and the electrode locations. In our application, the large width of the foam enforced a considerable distance between the non-neighboring electrodes, resulting in small electrical capacitances between them. This issue required a sensor design to address the practical limitations and reduce their effects on the ECT measurement signal.

In designing the ECT sensor, it was essential to have the electrodes on both the top and bottom surface of the foam. The simulation results predicted that the moisture on the bottom parts of the foam could not be detected without the bottom electrodes. Therefore, modifying the metallic table on which the conveyor belt was moving was required since the table prevented transmitting any signal from the bottom electrodes. Furthermore, since the thickness of the foam was only 30 mm, no electrodes were needed on the sides of the ECT sensor. The design of the developed ECT sensor is shown in Figure 18.

Six measuring electrodes are mounted on the top surface and another six measuring electrodes on the bottom surface of the ECT sensor. Since the foam was moving through the sensor, there was an air gap of 10 mm between the foam and the electrodes on the top surface of the sensor. Due to the large size of the electrodes, the air gap did not degrade the

This project has received funding from the European Union's Horizon 2020 research and innovation programme under the Marie Skłodowska-Curie Grant Agreement No. 764902.

reconstructions. The dimension of the sensor is $870\ \mathrm{mm}\ \times 250\ \mathrm{mm}\ \times 40\ \mathrm{mm}$. The height of the sensor is adjustable as the foam thickness can be different in the future experiments. Each measuring electrode is $100\ \mathrm{mm}\ \times 81\ \mathrm{mm}$, and the grounded electrodes located between every two adjacent measuring electrodes are $100\ \mathrm{mm}\ \times 3\ \mathrm{mm}$.

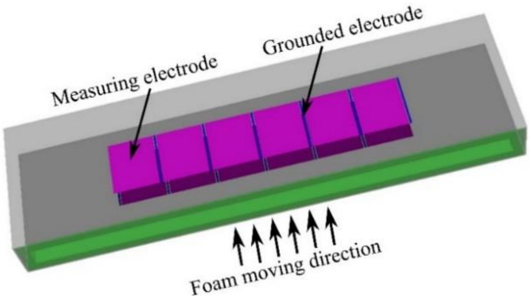

Figure 18: The ECT sensor design: Six measuring electrodes and six grounded electrodes on the top surface and the same number of electrodes on the bottom surface.

The sensor was connected to a measurement device built by Rocsole Ltd. Kuopio, Finland. The measurement device applied electrical voltage to the exciting electrodes and measured the inter-electrode capacitances. Each frame of measurements in ECT takes almost 720 ms. The measurements were transferred to a laptop connected to the device. The measured electrical capacitances were used in the reconstruction algorithm to estimate the permittivity distribution of the foam. Figure 19 shows the designed and built ECT sensor while connected to the measurement device and the laptop. The ECT sensor was then installed at the exit point of the microwave system, as shown in Figure 20.

5.3 Experimental results

Several experiments were conducted to estimate the moisture distribution of the polymer foams while moving via the conveyor belt. In this report, only the results of one of these experiments will be demonstrated. In this experiment, the microwave power sources were off, and the belt speed was set to 40 cm/min. Figure 21 shows a sample foam tested in this experiment. It contained 13 different pieces, which were cut, moisturized to certain amounts, and returned to their original locations in nine rows. While the foam moved through the electrode plane of the ECT sensor, 2D reconstructions were calculated at each time instant. In 2D reconstruction, it is assumed that the permittivity in the foam moving direction, is constant, and the permittivity distribution is reconstructed only in the cross-section of the target foam under the electrode plane.

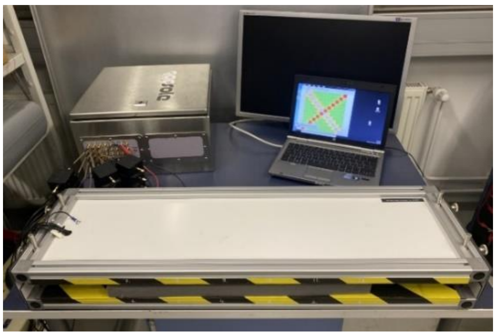

Figure 19: The ECT sensor while measuring the inter-electrode capacitances. A dry polymer foam is placed inside the sensor.

This project has received funding from the European Union's Horizon 2020 research and innovation programme under the Marie Skłodowska-Curie Grant Agreement No. 764902.

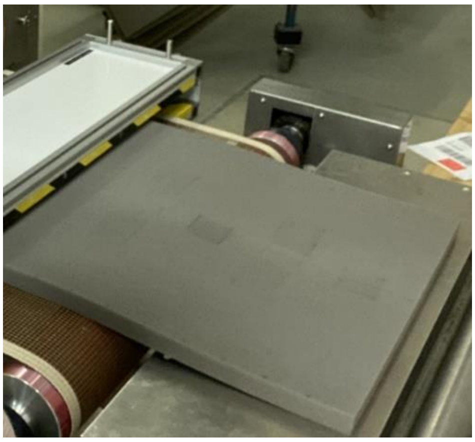

Figure 20: The ECT sensor installed on the microwave system while measuring the moisture distribution of a moving foam sample.

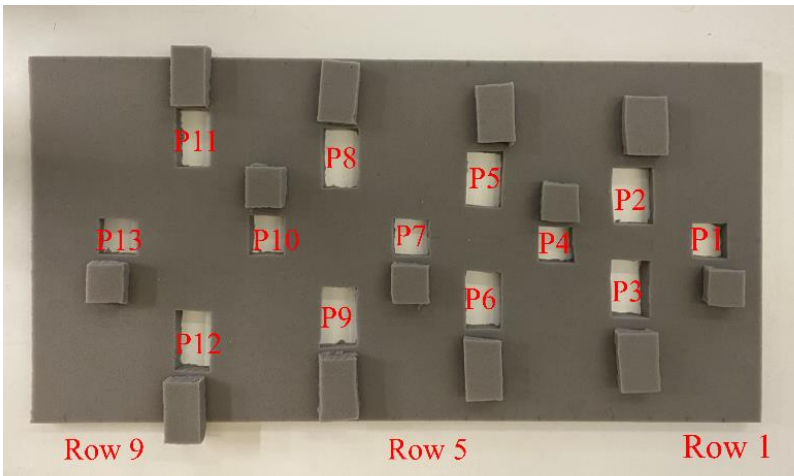

Figure 21: The sample foam tested for the measurements with 13 separate moisture locations.

A mapping between the actual moisture percentage of the pieces in the sample foam and the estimated permittivity change was obtained. The measured data, the fitted curve, and the 95 % prediction interval are shown in Figure 22. In this figure, M is the actual moisture percentage of pieces in the wet basis and $\Delta\epsilon_w$ is the normalized permittivity change percentage on the wet basis.

Figure 23 illustrates the 2D reconstructions at nine different time instants, in which each row of the sample foam was precisely in the middle of the electrode planes. The time variable, t, shows the time passed from the beginning of the experiment. The red rectangles in each figure indicate the actual locations of the moisturized pieces.

This project has received funding from the European Union's Horizon 2020 research and innovation programme under the Marie Skłodowska-Curie Grant Agreement No. 764902.

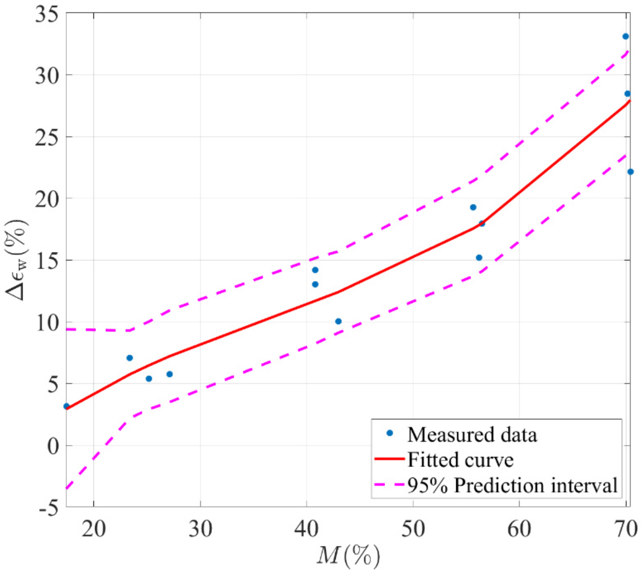

Figure 22: The mapping between the wet basis moisture percentage and the wet basis permittivity change percentage.

This project has received funding from the European Union's Horizon 2020 research and innovation programme under the Marie Skłodowska-Curie Grant Agreement No. 764902.

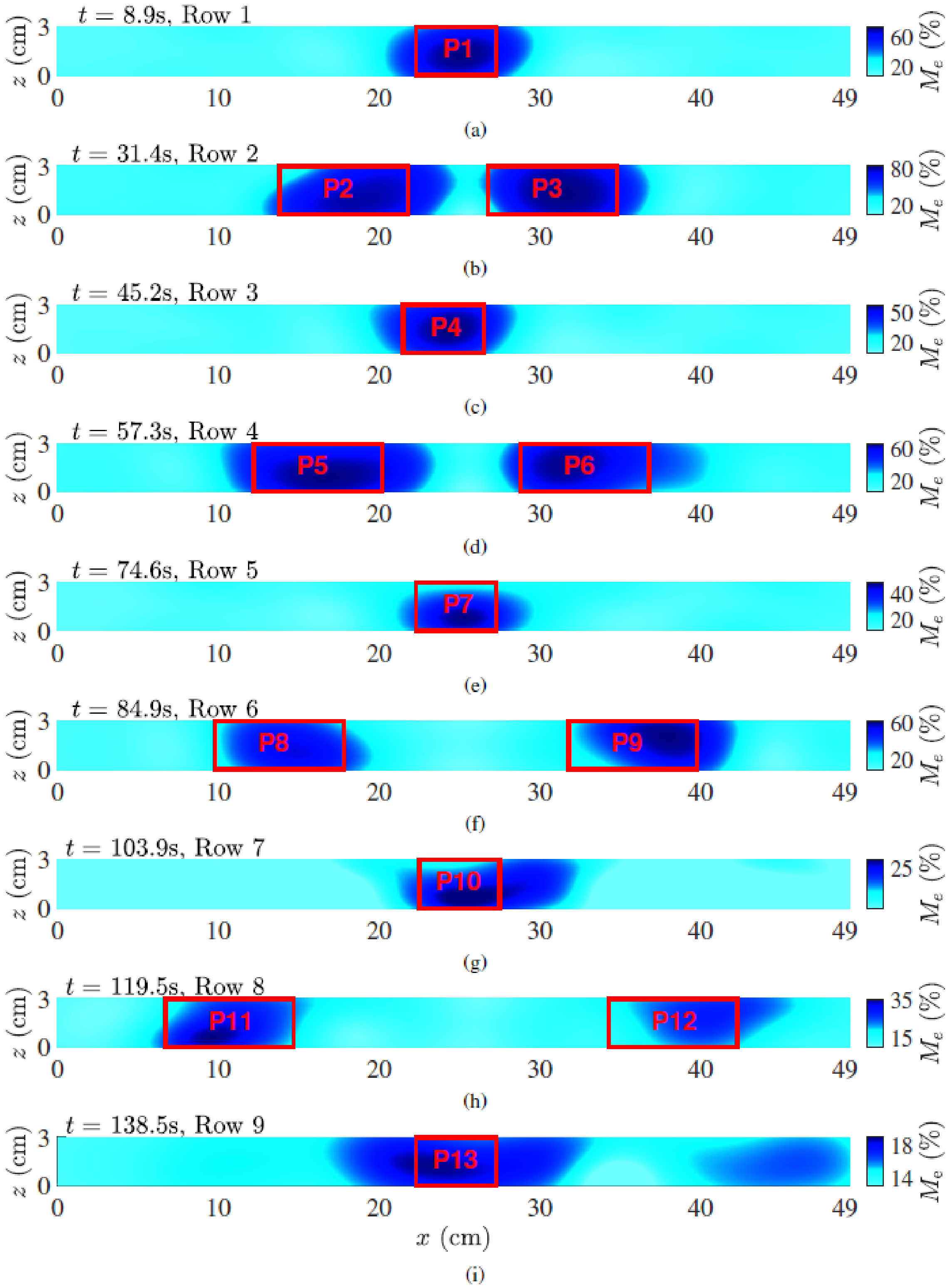

Figure 23: 2D reconstruction results from the dynamic experiment with the belt speed of 40 cm/min while the microwave sources were off. Each of the reconstructions is related to one of the rows in the sample foam when they passed through the electrode plane.

This project has received funding from the European Union's Horizon 2020 research and innovation programme under the Marie Skłodowska-Curie Grant Agreement No. 764902.

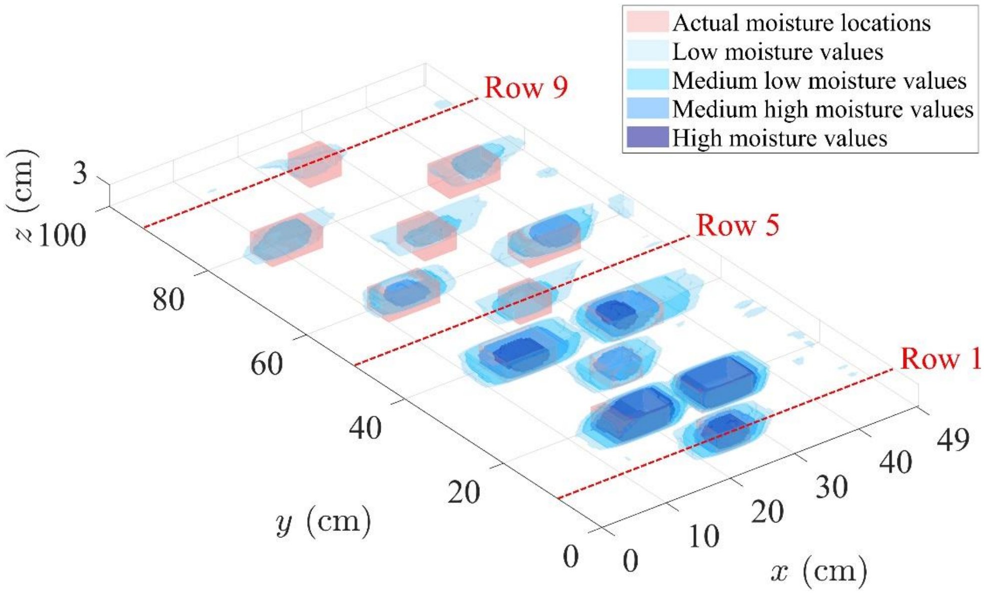

Figure 24: 3D visualization of the experiment results with a conveyor belt speed of 40 cm/min while the micro-wave sources were off.

All the 2D reconstructions from the experiment were stacked together to create a 3D visualization of these results, see Figure 24. As the pieces in this experiment had different moisture levels, four thresholds in the estimated moisture distribution were selected to show the variation in the moisture estimates more clearly.

5.4 Conclusion and further steps

The experimental results, in general, proved that the accuracy and the resolution of the ECT sensor are satisfactory, and this sensor is a suitable candidate for process control, which is one of the motivations of this research. The measurement time is short (almost 720 ms), and the reconstruction time also takes less than a second. Therefore, the measurements can be easily used in a closed-loop moisture control as the foam moisture feedback.

Currently, the measurements can be done in real-time. However, the reconstructions are calculated after the experiments as there is no communication between the measurement device and MATLAB software that runs the reconstruction algorithm. Therefore, the next step is establishing this connection. Furthermore, the moisture estimation error should be reduced to have a more accurate moisture control. One solution to decrease the error is by improving the calibration between the actual moisture and the estimated permittivity of the material.

This project has received funding from the European Union's Horizon 2020 research and innovation programme under the Marie Skłodowska-Curie Grant Agreement No. 764902.

6 Microwave tomography in industrial drying

A microwave tomography (MWT) module is integrated with the HEPHAISTOS industrial drying system, see Figure 25. The imaging modality is applied to estimate the moisture distribution in a polymer foam. Further, this information will be used as feedback for the moisture control of the microwave drying system, as shown in Figure 25. The MWT module and the proposed integration with the microwave system are illustrated in Figure 25. The physical principle, hardware implementation and data processing, reconstruction methods, and future steps of the MWT are described in the following sections.

6.1 Physical principle of microwave tomography

In MWT, the aim is to reconstruct the electrical properties and (or) the shape and size of an object by measuring its interaction with electromagnetic (EM) waves. Here, the operational frequency for the EM wave lies between 300 MHz and 300 GHz. In general, the measurement is performed by transmitting and receiving antennas. As for the reconstruction method, either quantitative or qualitative approaches are applied. Quantitative techniques give the electrical properties and shape of the object whereas the latter technique retrieve only the shape.

We apply MWT to estimate the moisture content distribution in a polymer foam. The sensor array consists of open-end waveguide antennas operating in the X-band range (from 8 GHz to 12 GHz). The sensor setup is fixed, and the sensor is placed above the foam. The schematic of the MWT system is shown in Figure 26. Since the foam is moving, the MWT measurement data acquisition and the reconstruction methods should be fast enough to estimate the moisture content distribution. A fast (and accurate) reconstruction method will provide sufficient reaction time for the control system to achieve selective heating in the drying process. The reconstruction time of less than one second is aimed at.

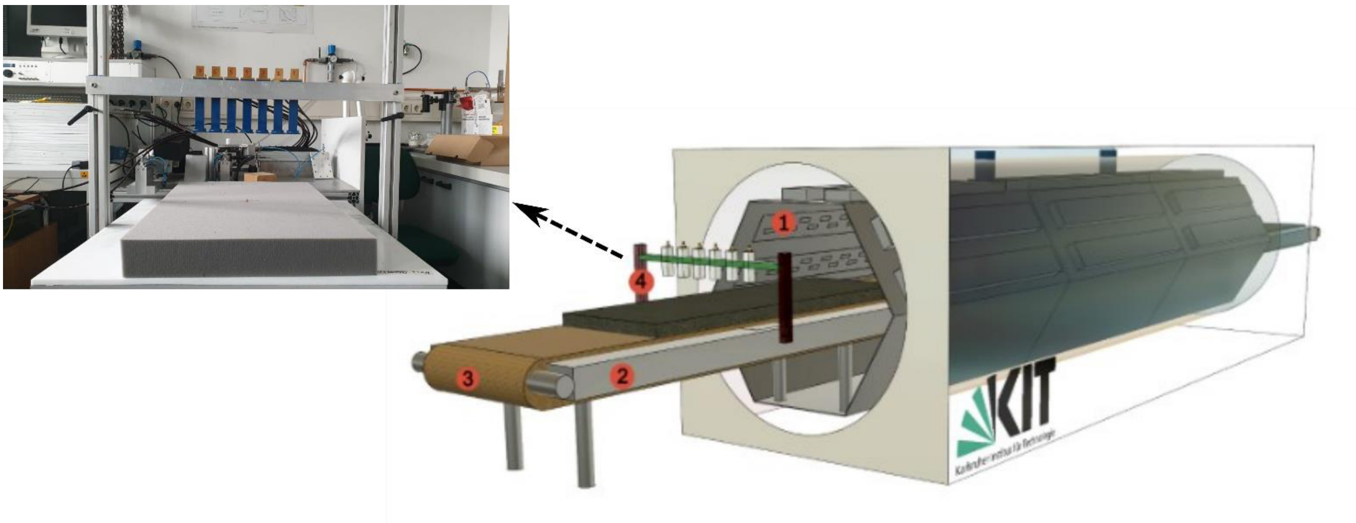

*Figure 25: **Right:** a schematic showing the proposed integration of the MWT module with the drying system. Main modules of the drying system are represented by number tags 1, 2, 3, and 4. Tag 1 represents the high-power microwave heating source, Tag 2 is the conveyor belt, and Tag 3 is the metal rod guiding element. MWT setup with waveguide antenna is represented by Tag 4. **Left:** the designed MWT module.*

This project has received funding from the European Union's Horizon 2020 research and innovation programme under the Marie Skłodowska-Curie Grant Agreement No. 764902.

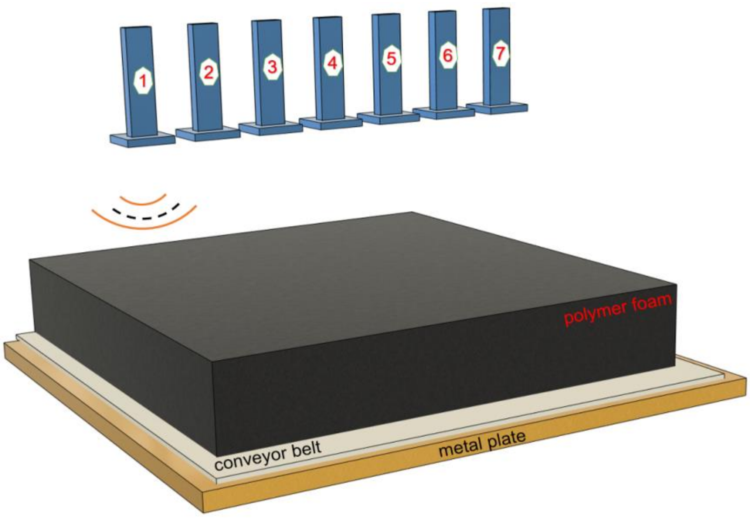

Figure 26: A schematic of the MWT system to estimate the moisture content distribution in the polymer foam. The MWT sensors consist of 7 open-end waveguide antennas operating in the X-band frequency range (from 8 GHz to 12 GHz).

6.2 Hardware implementation

The MWT imaging system consists of the following components:

i. X-band open-end waveguide antennas
ii. Phase-stable cables and a SubMiniature version **A** (SMA) connectors
iii. Switch
iv. Vector network analyzer (VNA)

Each component details are as follows.

S. No	Component	Specification	Description/Role
i	X-band open-end waveguide antennas 	Range: 8.2-12.4 GHz VSWR: 1.03:1 Insertion loss: 0.1	Antennas are used in the sensor array for MWT. They transmit and receive the signal and filter out the high-power electromagnetic leakage from the drying system.
ii	Microwave Phase stable cable (LU7-505-200) 	Frequency range: Up to 18 GHz Return Loss > 19 dB Connector1: SMA male Connector2: SMA male	These cables are used to connect VNA to the switch and the switch to the antennas.

This project has received funding from the European Union’s Horizon 2020 research and innovation programme under the Marie Skłodowska-Curie Grant Agreement No. 764902.

iii	2 ×16 USB Solid state switch matrix [5] 	Frequency: 300 KHz - 18 GHz	This device is connected to the VNA for more than two port measurement.
iv	Agilent N5224A (VNA) 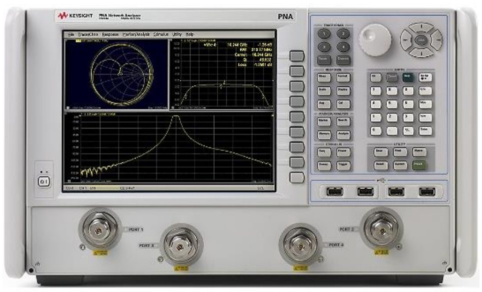	Two port network: Input and output Frequency range: 10 MHz - 43.5 GHz	This device is used for generating the monotone high-frequency signal. It measures the transmission and reflection loss of the MWT sensor antennas.

6.3 Data processing

For processing the data, the antenna sensor array is connected to the VNA via the solid state switch, see Figure 27. Since the VNA has only one input and one output port, the solid state switch is used to select the transmitter and receiver pair. The measurement is performed for all transmitting and receiving antenna pairs. We used the Instrument Control Toolbox in MATLAB for data acquisition. The measurement can be performed in the full X-band or at a single frequency.

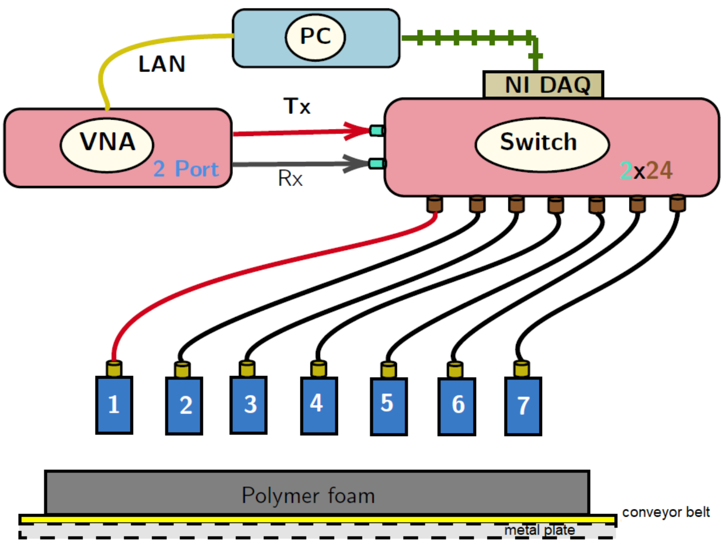

Figure 27: A schematic of the MWT measurement test bench.

This project has received funding from the European Union's Horizon 2020 research and innovation programme under the Marie Skłodowska-Curie Grant Agreement No. 764902.

A pseudo code for the data acquisition from the MWT measurement test bench is shown below.

Algorithm 1: MWT sensor data acquisition in MATLAB
Start: *Instrument Control Toolbox*
Input: *number of transmitter and receiver, N*

```
Call VNA_class ()          (open VNA connection)
for i = 1,2 ....... N
    for j = 1, 2......N
        Call Switch_class()
            Switch_class. open (i, j) –    (selection of input (Tx) and output (Rx) port)
            VNA_class. measure (S11, S12, S21, S22) –    (measure S-parameters)
    end
        Switch_class. close (i, j)
end
VNA_class. close ()
Switch_class. close ()
```

6.4 Reconstruction methods

6.4.1 Multi-static uniform diffraction tomography (MUDT)

A qualitative diffraction tomography based algorithm is proposed [6] for detecting the location of the moisture inside the polymer foam. Compared to the current qualitative imaging algorithm, the proposed algorithm provides a better spatial resolution using less antennas by employing only the non-diagonal elements of the measurement matrix. The reconstruction time is less than 1 second which is suitable for the real monitoring. Figure 28 shows an example of the reconstructed image with the proposed method.

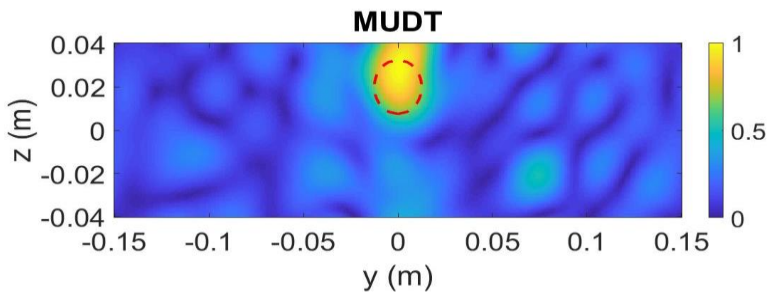

Figure 28: The reconstructed image for one potential moisture scenario in the foam with a cross-section size of 0.3 m x 0.08 m. The true location of the moisture is represented by the red dash line and the color bar indicates the normalized value of the moisture level.

This project has received funding from the European Union's Horizon 2020 research and innovation programme under the Marie Skłodowska-Curie Grant Agreement No. 764902.

6.4.2 Bayesian inversion framework and neural networks

A quantitative inversion framework using the Bayesian approach is tested with numerical data at 8.2 GHz [7]. From our feasibility study, it is observed that the method can estimate the inhomogeneous moisture distribution inside the foam and its wet-basis moisture content. However, the method is computationally heavy and time-consuming. Efforts to reduce the computational load are undertaken by coupling MUDT with the Bayesian approach [8].

We also developed an inversion framework based on neural networks [9]. The neural network was tested on numerical data and fulfills the targeted reconstruction time. The advantage of this method is that the network can be trained to recover the moisture content distribution from the scattered EM data generated using the three-dimensional (3D) forward model directly. Also, up to some degree of uncertainties in the measurements can be considered in the training data. Furthermore, the network can be trained on one suitable frequency or in the entire X-band frequency range.

6.5 Future steps

Our next steps are as follows:

i. Integrate the MWT imaging system with the industrial drying process and test its performance.
ii. Integrate the MWT with human computer interaction (HCI) module (**developed by ESR3**).
iii. Test the performance of the control block (**developed by ESR14**) with MWT.

6.6 References for microwave drying

[1] P. Pan, T. P. McDonald, B. K. Via, J. P. Fulton, J. Y. Hung, Predicting moisture content of chipped pine samples with a multi-electrode capacitance sensor, *Biosyst. Eng.*, Vol. 145, pp. 1–9, 2016.

[2] A. Voss, N. Hänninen, M. Pour-Ghaz, M. Vauhkonen, A. Seppänen, Imaging of two-dimensional unsaturated moisture flows in uncracked and cracked cement-based materials using electrical capacitance tomography, *Mater. Struct. Constr.*, Vol. 51, No. 3, 2018.

[3] W. Wang, K. Zhao, P. Zhang, J. Bao, S. Xue, Application of three self-developed ECT sensors for monitoring the moisture content in sand and mortar, *Constr. Build. Mater.*, Vol. 267, p. 121008, 2021.

[4] A. Voss, Imaging moisture flows in cement-based materials using electrical capacitance tomography, PhD thesis, University of Eastern Finland, 2020.

[5] P9164C 2X16 USB solid state switch matrix, 300 KHz to 18 GHz. [Online]. Available: https://www.keysight.com/de/pd-3052448-pn-P9164C/2x16-usb-solid-state-switch-matrix-300-khz-to-18-ghz?pm=PL&nid=-32739.1286686&cc=DE&lc=ger.

[6] A. Omrani, G. Link, J. Jelonnek, A Multistatic Uniform Diffraction Tomographic Algorithm for Real-Time Moisture Detection, *2020 IEEE Asia-Pacific Microwave Conference (APMC)*, pp. 437–439, 2020.

[7] R. Yadav, A. Omrani, M. Vauhkonen, G. Link, T. Lähivaara, Microwave tomography for moisture level estimation using Bayesian framework, *15th European Conference on Antennas and Propagation, EuCAP 2021*, 2021.

[8] A. Omrani, R. Yadav, G. Link, M. Vauhkonen, T. Lähivaara, J. Jelonnek, A combined

This project has received funding from the European Union's Horizon 2020 research and innovation programme under the Marie Skłodowska-Curie Grant Agreement No. 764902.

microwave imaging algorithm for localization and moisture level estimation in multilayered media, *15th European Conference on Antennas and Propagation, EuCAP 2021*.

[9] T. Lähivaara, R. Yadav, G. Link, M. Vauhkonen, Estimation of moisture content distribution in porous foam using microwave tomography with neural networks, *IEEE Trans. Comput. Imaging*, Vol. 6, pp. 1351–1361, 2020.

This project has received funding from the European Union's Horizon 2020 research and innovation programme under the Marie Skłodowska-Curie Grant Agreement No. 764902.

7 Continuous casting

For continuous casting, two different sensor modalities will be used: Contactless inductive flow tomography (CIFT) for the measurement of the two-dimensional flow field of the liquid metal in the mould and Mutual inductance tomography (MIT) for visualising the distribution of argon and liquid metal in the submerged entry nozzle (SEN).

7.1 Contactless inductive flow tomography (CIFT)

7.1.1 Physical principles

Contactless Inductive Flow Tomography (CIFT) is based on measuring the perturbations of an applied magnetic field due to the movement of a conductive fluid, and resolving the underlying linear inverse problem. If a fluid with a conductivity σ with the velocity $\boldsymbol{v}$ flows under the influence of an externally applied magnetic field $\boldsymbol{B}$, an electromotive force will be induced which drives a current $\boldsymbol{j}$ through the fluid according to the Ohm's law:

$$\boldsymbol{j} = \sigma(\boldsymbol{v} \times \boldsymbol{B} - \nabla\varphi)\,. \tag{8}$$

The current gives a rise to a magnetic field which can be calculated from Biot-Savarts' law:

$$\boldsymbol{b}(r) = \frac{\mu_0}{4\pi}\iiint_V \boldsymbol{j} \times \frac{\boldsymbol{r}-\boldsymbol{r}'}{|\boldsymbol{r}-\boldsymbol{r}'|^3}\,dV. \tag{9}$$

Under the assumption that the fluid boundary is insulating, the conversation of charges in the fluid must be preserved, thus the divergence of the current is zero:

$$\nabla \cdot \boldsymbol{j} = 0. \tag{10}$$

From (8) we obtain the Poissons' equation for the potential:

$$\nabla^2\varphi = \nabla(\boldsymbol{v} \times \boldsymbol{B}). \tag{11}$$

By substituting Equation (8) into Equation (9) and applying Gauss' theorem to express the potential term as the surface integral over the fluid boundary, and by resolving Equation (11), we obtain the following system of equations that calculates the flow induced magnetic field $\boldsymbol{b}$ at any location $\boldsymbol{r}$ from a given velocity field $\boldsymbol{v}$ inside volume V under the influence of the magnetic field $\boldsymbol{B}$:

$$\boldsymbol{b}(\boldsymbol{r}) = \frac{\mu_0\sigma}{4\pi}\iiint_V \frac{\big(\boldsymbol{v}(\boldsymbol{r}') \times \boldsymbol{B}(\boldsymbol{r}')\big) \times (\boldsymbol{r}-\boldsymbol{r}')}{|\boldsymbol{r}-\boldsymbol{r}'|^3}\,dV' - \frac{\mu_0\sigma}{4\pi}\oiint_S \frac{\varphi(\boldsymbol{r}')n(\boldsymbol{r}') \times (\boldsymbol{r}-\boldsymbol{r}')}{|\boldsymbol{r}-\boldsymbol{r}'|^3}\,dS'\ , \tag{12}$$

$$\begin{aligned}\varphi(\boldsymbol{r}) = \frac{1}{4\pi p(\boldsymbol{r})}\iiint_V &\frac{\big(\boldsymbol{v}(\boldsymbol{r}') \times \boldsymbol{B}(\boldsymbol{r}')\big) \cdot (\boldsymbol{r}-\boldsymbol{r}')}{|\boldsymbol{r}-\boldsymbol{r}'|^3}\,dV' \\ &- \frac{1}{4\pi p(\boldsymbol{r})}\oiint_S \frac{\varphi(\boldsymbol{r}')n(\boldsymbol{r}') \cdot (\boldsymbol{r}-\boldsymbol{r}')}{|\boldsymbol{r}-\boldsymbol{r}'|^3}\,dS'\ ,\end{aligned} \tag{13}$$

where $p(\boldsymbol{r})$ is a factor between $0 < p(\boldsymbol{r}) < 1$ determened by the shape of the boundary and depends on the solid angle of the surface at the position $\boldsymbol{r}$. dV' and dS' represent volume

This project has received funding from the European Union's Horizon 2020 research and innovation programme under the Marie Skłodowska-Curie Grant Agreement No. 764902.

and surface elements respectively. $\mathbf{B}(\boldsymbol{r})$ in general is a sum of the applied excitation magnetic field $\boldsymbol{B_0}(\boldsymbol{r})$ and flow induced magnetic field $\boldsymbol{b}(\boldsymbol{r})$, however since the ratio of the flow induced magnetic field and the applied magnetic field, defined by magnetic Reynolds number $Re = vl\mu_0\sigma$, is less than 1 we can presume that the $\mathbf{B}(\boldsymbol{r}) = \boldsymbol{B_0}(\boldsymbol{r})$. Then, the system of integral equations is linear in repect of the velocity.

By discretising the volume, V we can assemble the system of equations for each volume element and write it in following matrix form:

$$\boldsymbol{b} = \boldsymbol{R} \cdot \boldsymbol{v} + \boldsymbol{S} \cdot \boldsymbol{\varphi} \tag{14}$$

$$\boldsymbol{\varphi} = \boldsymbol{T} \cdot \boldsymbol{v} + \boldsymbol{U} \cdot \boldsymbol{\varphi} \tag{15}$$

Matrices $\boldsymbol{R}$ and $\boldsymbol{T}$ depend on the applied magnetic field $\boldsymbol{B_0}$, and matrices $\boldsymbol{S}$ and $\boldsymbol{U}$ depend only on the geometry of the system. From the matrix system of equations, we arrive to the relation between the fluid velocity $\boldsymbol{v}$ and the flow induced magnetic field $\boldsymbol{b}$:

$$\boldsymbol{b} = \boldsymbol{M} \cdot \boldsymbol{v}, \tag{16}$$

Where matrix $\boldsymbol{M}$ is given by:

$$\boldsymbol{M} = [\boldsymbol{R} + \boldsymbol{S}((\boldsymbol{I} - \boldsymbol{U})^{-1,defl})\boldsymbol{T}]. \tag{17}$$

The non-uniqueness of the underlying linear problem is resolved by Tikhonov regularization. We seek to minimize the following expression:

$$\min_{v}\{\|\boldsymbol{M} \cdot \boldsymbol{v} - \boldsymbol{b}\|_2^2 + \lambda\|\boldsymbol{G} \cdot \boldsymbol{v}\|_2^2 + \lambda_D\|\nabla\boldsymbol{v}\|_2^2\}. \tag{18}$$

Here, $\lambda_{\mathrm{D}} = 1$ and the value of the regularisation parameter λ is determined by the L-curve method.

7.1.2 Hardware implementation

The excitation magnetic field is generated by two rectangular coils, which are stacked in axial direction. The coils generate the magnetic field in the vertical direction. Each coil has six windings of 7×4 mm copper wire to minimize the ohmic losses. The distance between the coils is 57 mm. The arrangement of the excitation coils is shown in Figure 29.

This project has received funding from the European Union's Horizon 2020 research and innovation programme under the Marie Skłodowska-Curie Grant Agreement No. 764902.

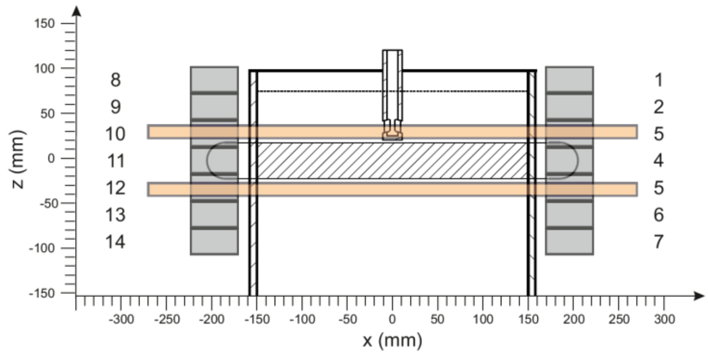

Figure 29: Arrangement of the excitation coils, sensor arrays and electromagnetic brake (EMBr) in relation to the SEN and the mould.

The coil is fed with an alternating current of 25 A with a variable frequency in the range from 1 Hz to 20 Hz. The amplitude of the excitation magnetic field is 1.55 mT at the center between both coils for 25 A. The measurement of the magnetic field and the results from the numerical simulations along the z axis is given in Figure 30.

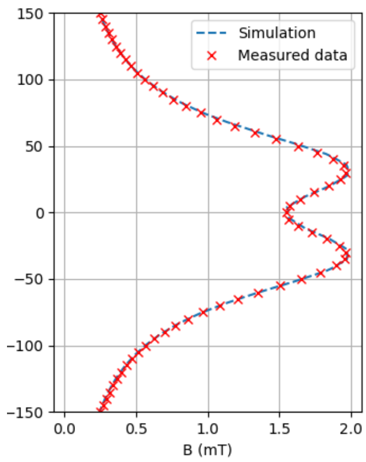

Figure 30: Measured and simulated excitation magnetic field along the z-axis. Height 0 is the middle distance between two excitation coils.

The flow-induced magnetic field is measured by fourteen gradiometric sensors, seven at each narrow side of the mould as shown in Figure 29. Gradiometric coils consist of two individual coils of 160 000 windings of $25\ \mu m$ wire wound in opposite direction and connected in series. With this method, the gradient of the magnetic field in the axial direction of the coil is measured. Additionally, this configuration eliminates the effects of magnetic fields that are uniform along the axis of the sensor since the induced voltage in two individual coils is exactly the same in value but opposite in polarity. Figure 31 shows the sketch of the gradiometric coil.

This project has received funding from the European Union's Horizon 2020 research and innovation programme under the Marie Skłodowska-Curie Grant Agreement No. 764902.

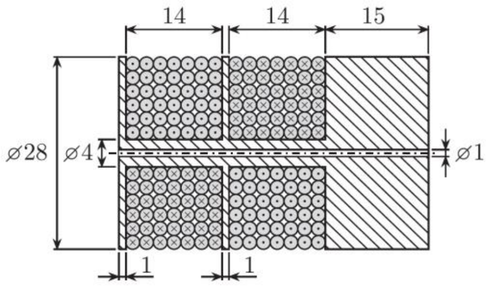

Figure 31: Sketch of the gradiometric coil used for the measurement of the flow induced magnetic field. All values in mm [1, 2].

The acquisition of the voltage induced in the gradiometric coils as well as the acquisition of the current through the excitation coils are done with a LTT24 24-bit A/D converter from Tasler shown in Figure 32a. Figure 32b shows the photograph of the assembled CIFT setup with one additional gradiometric coil.

a) *b)*

Figure 32: Measurement acquisition device (a) and assembled excitation coil and sensor array on the Mini-LIMMCAST facility (b).

7.1.3 Data processing

The data is sampled with the frequency of 5 kHz with a 24-bit resolution. The sampling frequency is chosen well above Nyquist frequency for the low frequencies of the excitation field. The measured voltage is then decomposed in in-phase and out-phase components by using Lomb-Scargle procedure. The in-phase component of the measured voltage contains the information of the perturbations caused by the flow i.e. $v \times B$ term in (8). Following the demodulation of the signal, voltages are converted to the magnetic field based on the transfer function of the gradiometric coil for each sensor. The out-phase component contains the information of the time varying magnetic field of the AC excitation magnetic field. At the beginning of the measurement, the in-phase component is zeroed out, thus any deviation from the zero is the signal generated by the flow. Figure 33 shows the example of the flow induced magnetic field for one experiment.

This project has received funding from the European Union's Horizon 2020 research and innovation programme under the Marie Skłodowska-Curie Grant Agreement No. 764902.

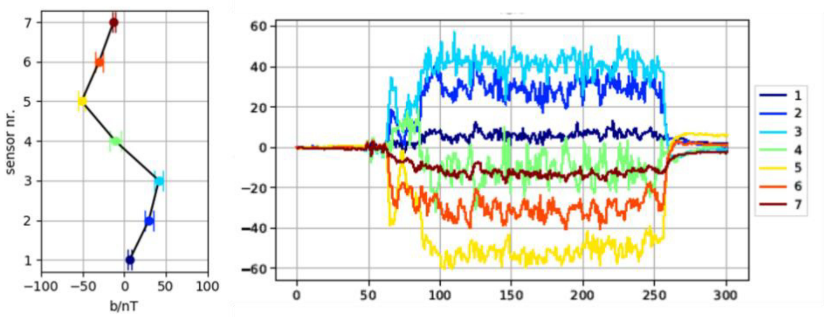

Figure 33: Flow induced magnetic field for sensors 1 - 7.

From the information of the flow induced magnetic field the velocity field can be reconstructed by solving the inverse problem. An example of the reconstructed velocity field from one experiment is given in Figure 34.

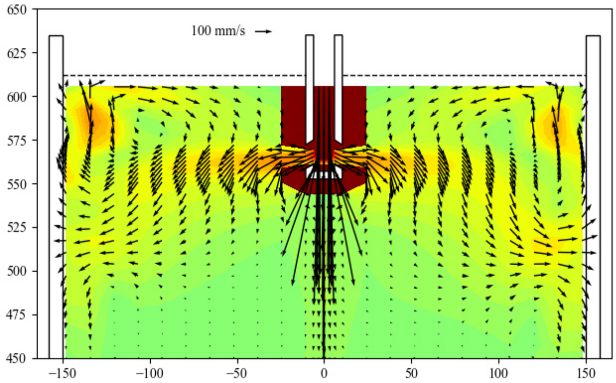

Figure 34: Reconstructed velocity based on the magnetic field measurement shown in Figure 33.

7.1.4 Implementation in process spaces

Contactless inductive flow tomography is assembled and used with a laboratory model of the continuous caster Mini-LIMMCAST. The Mini-LIMMCAST model is operated with eutectic alloy Gallium-Indium-Tin (GaInSn) which is liquid at room temperature. GaInSn has properties similar to the properties of liquid steel. The mould of the laboratory model is made of acrylic glass and it has a rectangular profile $300 \times 35\ mm$. The ratio of the size of the laboratory model of the mould and the one used in industry is roughly $1:4$. The position of CIFT on the setup is determined by the position of the Electromagnetic Brake (EMBr) as the excitation coils for CIFT are attached to it. The EMBr is positioned $77\ mm$ below the free surface of the liquid metal, where the influence of the EMBr on the flow structure in the mould is the highest [3]. This position also corresponds to the middle point between the two excitation coils and is shown in Figure 29.

The Purpose of CIFT is to provide the information to the controller about the velocity field in the mould when influenced by the EMBr. The controller is designed to change the magnetic field of the EMBr in order to achieve desired flow conditions. This is done by extracting specific features from the velocity field such as the angle of the jet leaving the SEN. The principal structure of the control loop used in the demonstrator is given in Figure 35.

This project has received funding from the European Union's Horizon 2020 research and innovation programme under the Marie Skłodowska-Curie Grant Agreement No. 764902.

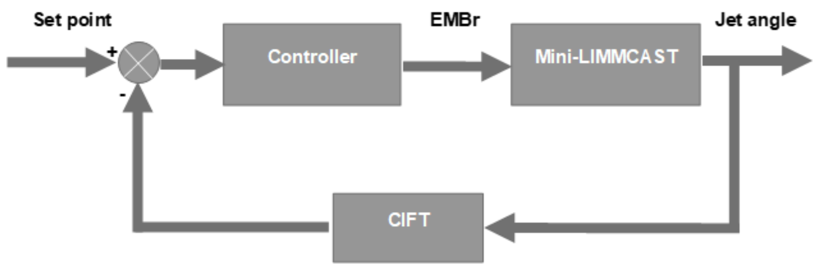

Figure 35: Control loop.

In order to continuously provide data for the controller, a subsequent real time implementation of the velocity reconstruction has been realized. Real time reconstruction is based on precalculating the inverse of the resulting matrix for a set of different values of the regularization parameter λ. This reduces the reconstruction to matrix-vector multiplications instead of solving linear equations for different values of the regularisation parameter [4].

7.1.5 Performance analysis

The performance of the CIFT reconstruction can be measured in accuracy of the reconstruction, time needed per frame of reconstruction, and based on the mechanical robustness of the setup.
By mounting the CIFT setup firmly on the EMBr, a significant increase in the robustness of the measurement setup was achieved. However, by mounting the CIFT sensor on the EMBr effects of temperature changes of the yoke of the EMBr can be observed.
Real-time reconstruction by pre-calculating the inverse of regularization matrices shows a great improvement in time required for each measurement frame [4]. Experiments show that the regularization parameter λ does not differ significantly from one time step to another, and thus the initialization of the regularization matrices can be computed beforehand, shifting the computational load of calculating the matrix inverse away from measurement time. At the measurement time, it is only necessary to perform a series of matrix-vector multiplications, which can be executed within several milliseconds as opposed to minutes required for the matrix inversion used for reconstruction.

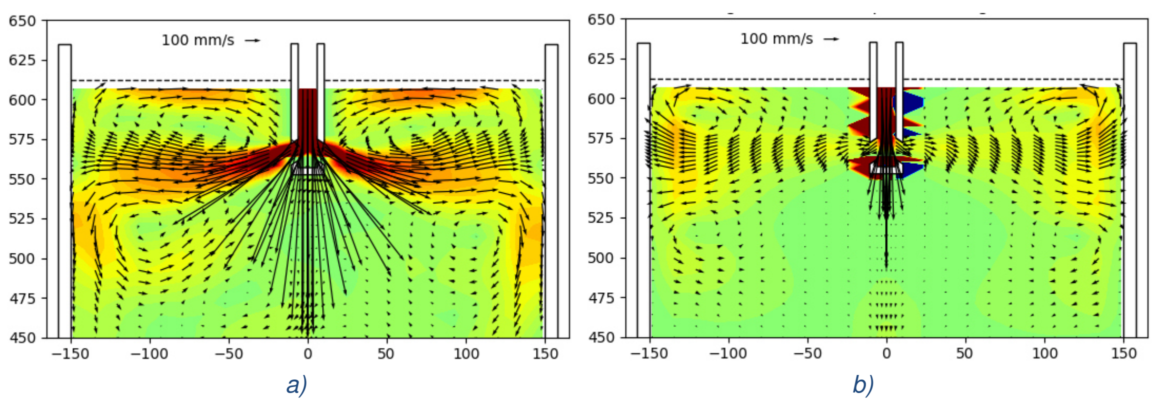

Figure 36: Velocity field calculated by numerical simulation used to generate the flow induced magnetic field (a), and reconstructed velocity field from that flow induced magnetic field (b).

This project has received funding from the European Union's Horizon 2020 research and innovation programme under the Marie Skłodowska-Curie Grant Agreement No. 764902.

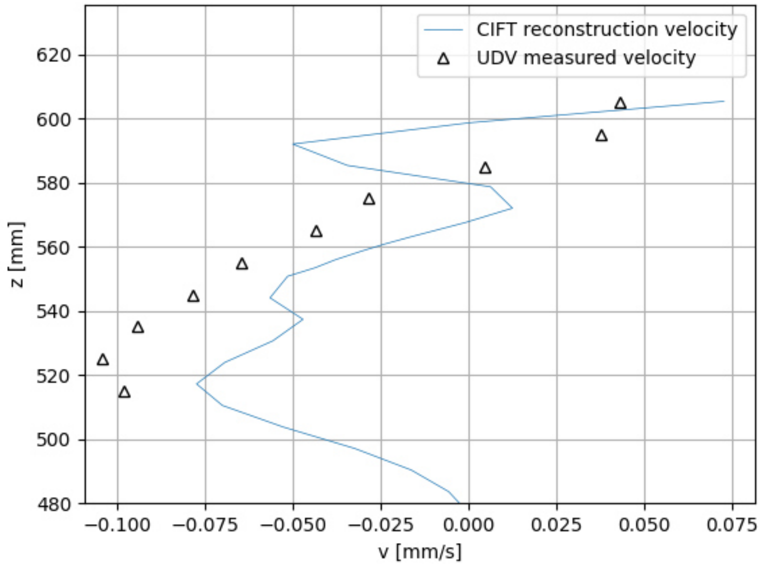

Figure 37: Comparison of reconstructed velocities from CIFT and UDV along the vertical line at x = -134.2 mm.

Quantifying the accuracy of the reconstruction can be done by starting from a simulated velocity field, calculating the flow induced magnetic field and finally, reconstructing the flow based on the simulated magnetic field. After this procedure, the reconstructed and the original velocity field can be compared. As an example, Figure 36a shows the simulated velocity field and Figure 36b the reconstructed velocity field. The quality of the reconstruction can also be determined by comparing the reconstructed velocities from the experiments to the velocities measured by the ultrasound Doppler velocimetry (Figure 37).

7.1.6 References for continuous casting, CIFT

[1] M. Ratajczak and T. Wondrak, Analysis, design and optimization of compact ultra-high sensitivity coreless induction coil sensors, *Measurement Science and Technology,* Vol. 31, No. 6, 2020.

[2] M. Ratajczak, T. Wondrak, F. Stefani, A gradiometric version of contactless inductive flow tomography: theory and first applications, *Philos Trans A Math Phys Eng Sci,* Vol. 374, No. 2070, 28th June 2016.

[3] D. Schurmann, I. Glavinić, B. Willers, K. Timmel, S. Eckert, Impact of the Electromagnetic Brake Position on the Flow Structure in a Slab Continuous Casting Mold: An Experimental Parameter Study, *Metallurgical and Materials Transactions B,* Vol. 51, No. 1, pp. 61-78, 2019.

[4] T. Wondrak, R. T. Jacobs, P. Faber, Fast Reconstruction Algorithm for Contactless Inductive Flow Tomography, (in English), *2020 10th International Conference on Advanced Computer Information Technologies (Acit),* pp. 217-220, 2020.

This project has received funding from the European Union's Horizon 2020 research and innovation programme under the Marie Skłodowska-Curie Grant Agreement No. 764902.

8 Mutual inductance tomography (MIT) in continuous casting

8.1 Physical principles

An approach is established to extract the conductivity in the sensing area. It uses eddy current field measurement to distinguish the object in contrast with the background field. The MIT principle is depicted in Figure 38, where a coil is excited by current *I* (red arrows), whereas the other coil is induced by voltage *V* because of ***A*** field (surface plot) in the region with the distribution of conductivity *σ* and eddy current (black arrows) [1].

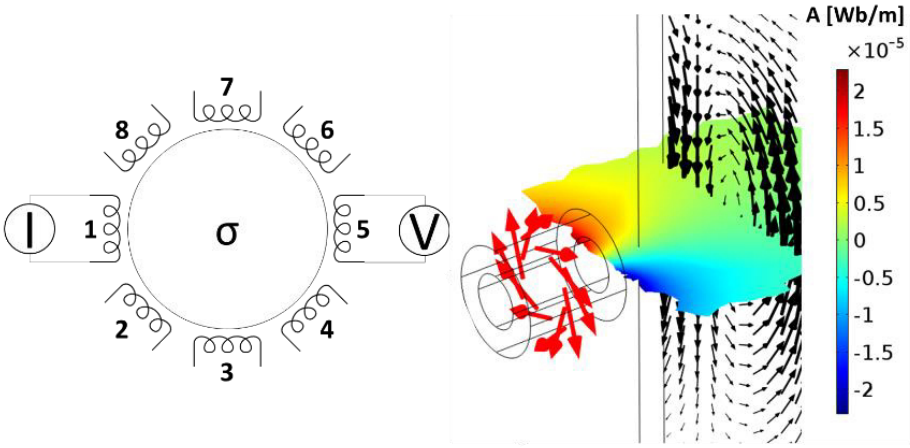

Figure 38: MIT measurement principle.

The magnetic vector potential is defined to form the given governing equation of eddy current, where *μ* is permeability, ***A*** is the magnetic vector potential, *ω* is the angular frequency of the current in the coil, *σ* is the electrical conductivity, and $\boldsymbol{J_s}$ is the excitation current density.

$$\nabla \times \frac{1}{\mu} \nabla \times \boldsymbol{A} + j\omega\sigma\boldsymbol{A} = \boldsymbol{J_s} \tag{19}$$

Therefore, MIT sensors' outputs are induced voltage (*V*) on the detector coils (k) due to the magnetic field (***B***) generated by the exciter coil and the secondary field from the eddy current which occurs on the conductive object in the sensing area.

$$V = -k\frac{d\boldsymbol{B}}{dt} \tag{20}$$

Through reconstruction, MIT reveals a spatial image of conductivity distribution in the sensing space. The inversion process obtains the pixelated conductivity ***K*** from the set of boundary measurements ***V***, and is solved using various algorithm, e.g. Tikhonov, employing the transformation matrix (Jacobian) ***J***.

$$\boldsymbol{V} = \boldsymbol{JK} \tag{21}$$
$$\boldsymbol{K} \approx (\boldsymbol{J^T J} + \lambda \boldsymbol{R})^{-1} \boldsymbol{J^T V} \tag{22}$$

where ***R*** and *λ* are the regularisation matrix and regularisation parameter, respectively. The Jacobian ***J*** is formulated from prior forward computation using the finite element method (FEM), and the spatial size is in cross-sectional 2D 50-by-50 pixels.

This project has received funding from the European Union's Horizon 2020 research and innovation programme under the Marie Skłodowska-Curie Grant Agreement No. 764902.

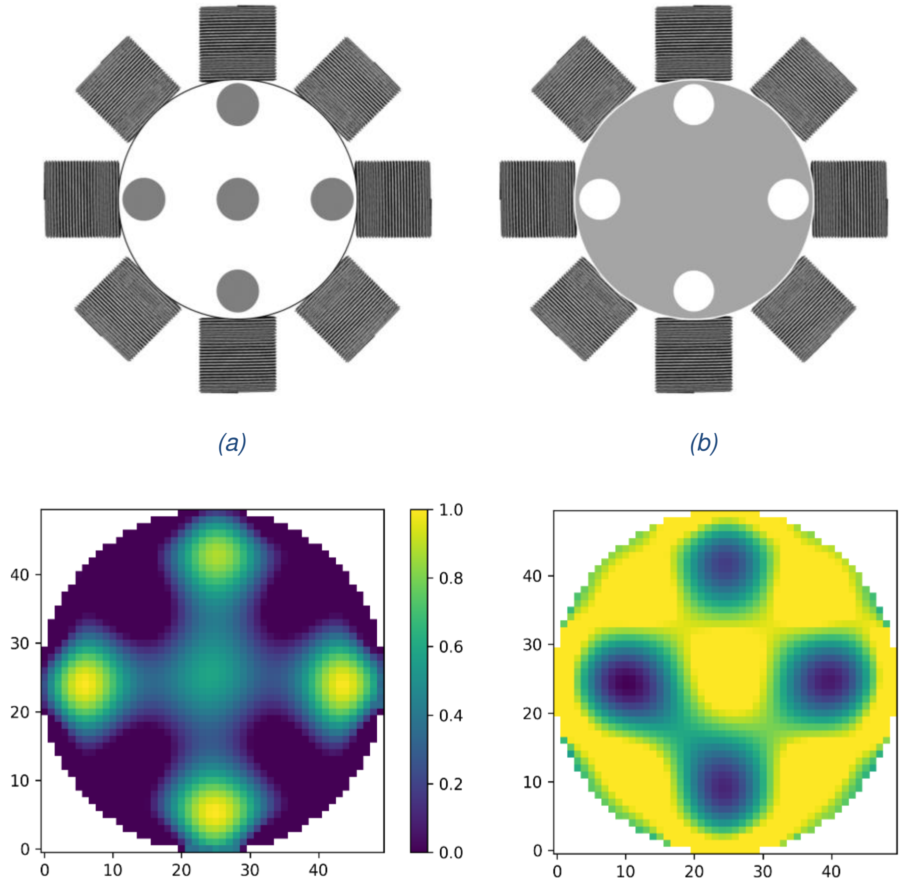

Figure 39: Image reconstruction performance: a) 5 copper rods (d = 5mm) in air-background (D = 50 mm), b) 4 wood sticks (d = 5 mm) in GaInSn-background (D = 50 mm).

Figure 39 shows examples of image reconstruction results based on experiments [2] for both conductive objects against non-conductive background (a) as well as non-conductive objects against conductive background. Here the values are scaled/normalised into min-max 0-1. The overall sensitivity is stronger near the sensors (at the edges of the region of interest) and weak at the centre. Consequently, the centrally located object (in Figure 39a) has a relatively smaller reconstructed value although the actual conductivity value is equal with the others. Similarly, the object' dimension in the reconstructed image is also affected by the spatial sensitivity and regularisation parameters.

8.1.1 Hardware implementation

Tomographic data are formed as arrays of sensors' measurement combination. In the case of 8 sensors in Figure 40, each of which can act as either exciter or detector, one frame (a complete set of 'projection') consists of 28 voltages reading arrangement as shown in Table 1.

This project has received funding from the European Union's Horizon 2020 research and innovation programme under the Marie Skłodowska-Curie Grant Agreement No. 764902.

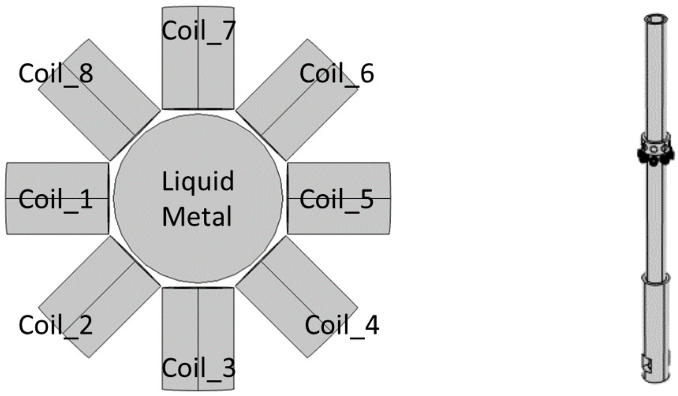

(a) *(b)*

Figure 40: Tomographic sensor configuration: a) top view with liquid metal object, b) installation on the SEN.

Table 1: Measurement index for 8-sensor

Measurement index		Detector						
		coil_2	coil_3	coil_4	coil_5	coil_6	coil_7	coil_8
Exciter	coil_1	1	2	3	4	5	6	7
	coil_2		8	9	10	11	12	13
	coil_3			14	15	16	17	18
	coil_4				19	20	21	22
	coil_5					23	24	25
	coil_6						26	27
	coil_7							28

The sensor's construction consists of three parts: Coil, case/housing, and connector/port (Figure 41). Each coil is made of wire-wound (32 AWG) with an outer diameter of 5 mm and a length of 5 mm. It has a ferrite-core of 2.5 mm in diameter and 8 mm in height. The circular assembly is divided into two sections for convenient installation on the mini-LIMMCAST SEN, where a section contains four coils housed inside a plastic case. On the front, arc's (half-circle) diameter is 16 mm to suit the SEN dimension; at the rear, a DB9 connector is placed for extension cable to the electronics; and additional side-wings are meant for securing the body.

This project has received funding from the European Union's Horizon 2020 research and innovation programme under the Marie Skłodowska-Curie Grant Agreement No. 764902.

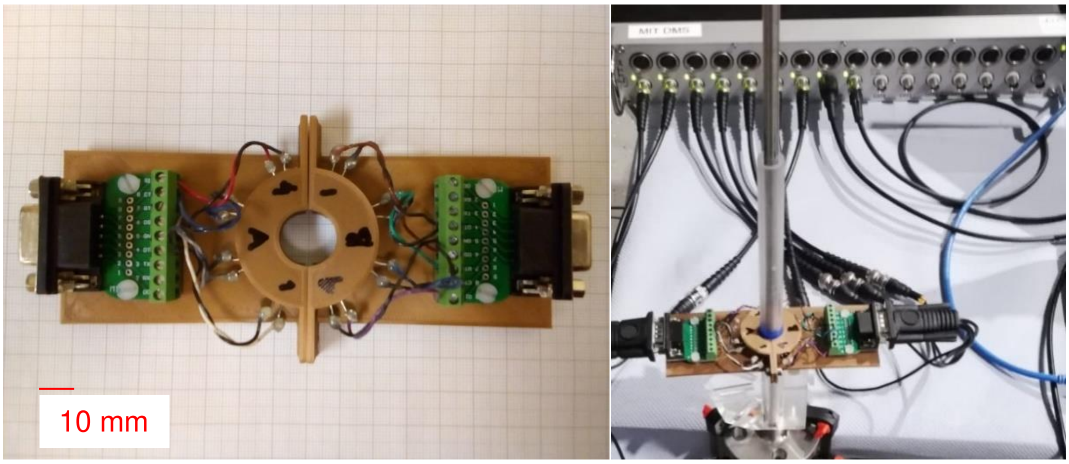

(a) *(b)*

Figure 41: Sensor construction (a) and calibration test (b).

The measurement is taken sequentially for every mutual pairs (coil-combination of exciter-detector) in counter-clockwise direction. For example, according to the arrangement in Figure 41, the coil A1 is injected with ac current of 1 mA (f = 100 Hz) and induced voltages are measured on coil B4, B3, B2, …, and A2 for the first turn. Subsequently, coil B4 is injected, and voltages are measured on coil B3, …, and A2 for the second turn, and so on until the seventh turn. For simplicity, the reverse-pairings can be neglected (e.g., A1-B4 pair is considered similar with B4-A1 pair). These sequences are controlled by multiplexing instrument.

8.1.2 Data processing

The MIT system provides a continuous data stream of 2D-array [Nx28], i.e., N number of complete projection data (28 voltage values). The row is associated with timestamp of the measurement, and its size depends on the pre-defined buffer recording and/or start-stop trigger commands.

$$DAT = \begin{bmatrix} V_{1,1} & \cdots & V_{1,28} \\ \vdots & \ddots & \vdots \\ V_{N,1} & \cdots & V_{N,28} \end{bmatrix} \tag{23}$$

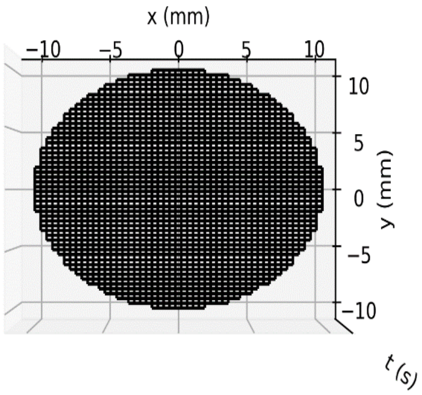

Figure 42: Spatio-temporal pixelated 2D image form.

This project has received funding from the European Union's Horizon 2020 research and innovation programme under the Marie Skłodowska-Curie Grant Agreement No. 764902.

Then, the inverse problem will be solved in post-processing computer. This procedure transforms the data into a spatio-temporal pixelated 2D image as illustrated in Figure 42. The raw data and the reconstructed images will be presented via a TCP/IP server. The file contains the array data and the conductivity distribution, which is stored as a list of coordinates with the gas/liquid information as scalar field. The scalar field is a binary field, where '0' represents the liquid metal and '1' represents the gas. Alternatively, the flow regime or gas-liquid area fraction is quantified. The expected time resolution will be about 100 frame-per-second (fps).

8.1.3 Implementation in process spaces

Figure 43 shows the planned setup for implementation in the demonstrator. The hardware consists of ac current source at transmitter (Tx) line; instrumentation amplifier, bandpass filter, output gain at receiver (Rx) line; and an analogue multiplexer for switching the coils to operate either in Tx or Rx mode. The designed MIT system has a signal-to-noise ratio (SNR) of 60 dB at an operating signal frequency of 130 Hz.

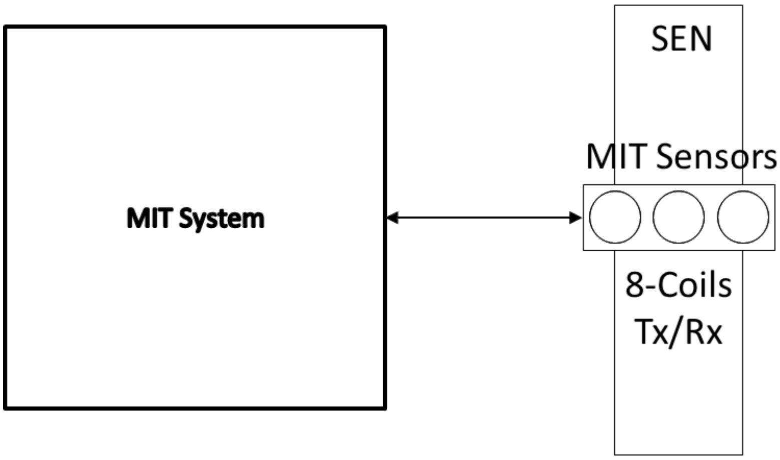

Figure 43: Setup for the demonstrator.

Firstly, prior calibration on the sensing-space has to be done as reference (background) data. The aforementioned measurement procedure is taken in condition where the sensing area is empty. The resulting calibration data is (typically) only valid for the immediate running session. Here the position of the coil number/index should be marked against the SEN side (for spatial coordinate in the reconstructed image) and kept intact for the following measurement session.

On the run (once flow starts), commands are sent to trigger the synchronous recording along with visual observation and CIFT measurement. Any change of process' parameters (stopper, argon, electromagnetic break) should be timely noted for correlation.

8.1.4 Performance analysis

A static test has been done with the sensor using a predefined flow-shape GaInSn-gas filling profile: Part-filled, fully filled and bubbly/voids. The image quality is further affected by regularisation. A qualitative approach is taken where a high image value relates with a high estimation of conductivity.

This project has received funding from the European Union's Horizon 2020 research and innovation programme under the Marie Skłodowska-Curie Grant Agreement No. 764902.

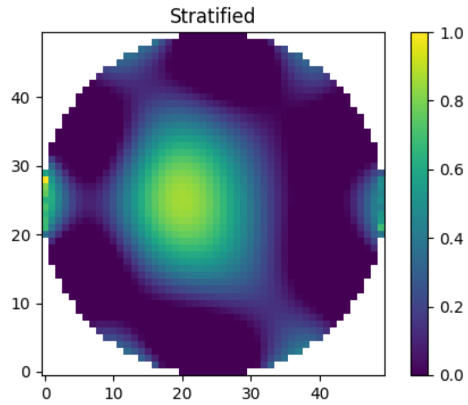

(a)

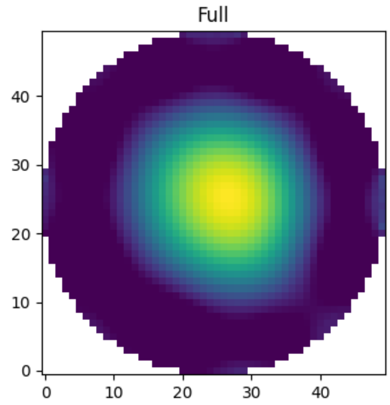

(b)

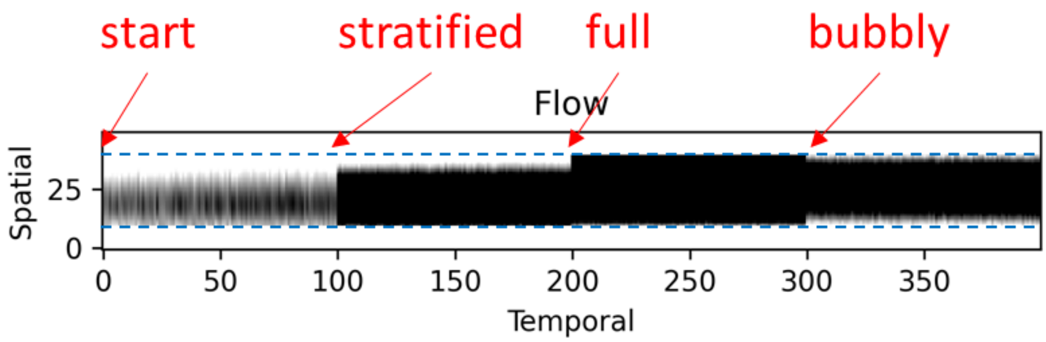

(c)

Figure 44: Flow imaging example.

The reconstruction result is shown in Figure 44. Note that as the sensors also encapsulate the wall and outer area, the inner SEN zone is located from (10,10) to (40,40) in the spatial axes (X,Y). The top figures (Figure 44a and Figure 44b) depicting cross-sectional image (50x50 pixels); whereas the bottom figure (Figure 44c) illustrating a spatio-temporal image-slice at the centre of one of the spatial axes (X=25) with a blue dashed-line indicating the SEN interior. In the latter, the temporal axis is a sample number (n) with a frame rate of 0.1 fps. Having applied the thresholding value, the colourmap is a binary field of liquid (1) and gas (0) regime. The flow starts at n = 0, changes to stratified (n=100), full (n=200) and then bubbly/voids at n = 300. Putting into the same scale, at the beginning there is small amount of liquid metal, hence low (almost noisy) image value. At the stratified stage, the interface between the liquid-gas is clearly depicted. For a full, strong signal resulting in a very pronounced image. Afterwards, voids ('gas') are introduced at the centre (Y=25) and both edges (Y=10; Y=40). However, they are not distinctive in the image. Figure 16c is a reconstruction from the pre-collected measurement data. Having fixed Jacobian, regularisation matrix, and parameter, the abovementioned performance is assumed for online processing. A set of 28-voltage reading takes about 10 s to be stored in software buffer. This is mainly due to hard-

This project has received funding from the European Union's Horizon 2020 research and innovation programme under the Marie Skłodowska-Curie Grant Agreement No. 764902.

ware electronics and interfacing latency. The Tikhonov algorithm execution for 400 images takes approximately 5 s using computation resources: 1 GB of RAM in dual-core CPU at 2.30 GHz.

8.1.5 References for continuous casting, MIT

[1] I. Muttakin, T. Wondrak M. Soleimani, Magnetic Induction Tomography Sensors for Quantitative Visualization of Liquid Metal Flow Shape, *IEEE Sensors Letters*, Vol. 4, No. 7, pp. 1-4, July 2020, Art no. 6001204, doi: 10.1109/LSENS.2020.3000292.

[2] I. Muttakin and M. Soleimani, Noninvasive Conductivity and Temperature Sensing Using Magnetic Induction Spectroscopy Imaging, *IEEE Transactions on Instrumentation and Measurement*, Vol. 70, pp. 1-11, 2021, Art no. 4500211, doi: 10.1109/TIM.2020.3016435.

This project has received funding from the European Union's Horizon 2020 research and innovation programme under the Marie Skłodowska-Curie Grant Agreement No. 764902.

9 Batch crystallization

9.1 Ultrasound tomography in batch crystallization

For the batch crystallization process, an Ultrasound computed tomography (USCT) transmission approach was implemented. This reconstruction method is based on the direct transmitted pulses and measures the time-of-flight (TOF) of the first-arrival pulse. This type of tomography is useful for processes that use substances in the same material phase in which the acoustic impedance does not dramatically change, being suitable for ultrasonic signal transmission.

The model system for constructing USCT is a calcium carbonate precipitation using calcium chloride and sodium carbonate. For the demonstration development, this approach is considered sufficicient to cover the precipitation process via feeding a carbonate solution as a semi-batch precipitation.

9.1.1 System and sensors design

The proposed USCT system consists of an array of multiple piezoelectric sensors, a sensing electronics setup for data acquisition and a computer system for image reconstruction. The system consists of a ring of 32 piezoelectric transducers circle-wise and it is meant to be used in stirred industrial tanks concept, as depicted in Figure 45. The sensors are mounted on the tank and use a centre frequency of 40 kHz and a sound pressure level of close to 97 dB (30 cm/10V rms). The reason of choosing such a frequency is quite important and is related to the directivity of the emission of the sensors. Piezoelectric transducers have a specific pattern of emission which is related to the way that they are constructed. Moreover, as long as the frequency is going higher, the pattern of directivity of the sensor becomes narrower. Thereafter the angle beam of emission in every single emission frame is decreasing and subsequently the region-of-interest (ROI) is being scanned sparsely. Concluding, it seems that sensors of few MHz are inappropriate for a tomographic application because of their narrow directivity. Sensors of few hundred kHz and lower seem more appropriate.The sensors are attached in the outer surface of it, being non-destructive, and therefore the pulse travels through the tank for a distance equal to its thickness. It is important to use a “friendly” acoustic material for the tank because the pulse has not to lose a big amount of its power by travelling through the tank.

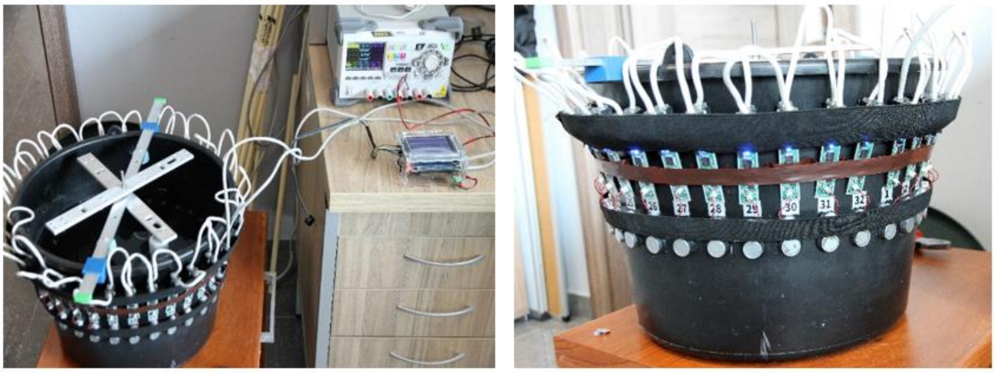

Figure 45: The developed ultrasonic system. A ring of 32 piezoelectric transducers mounted to the black bucket.

This project has received funding from the European Union’s Horizon 2020 research and innovation programme under the Marie Skłodowska-Curie Grant Agreement No. 764902.

The concept of the developed ultrasound tomograph assumes the construction of active measurement probes controlled by an external module via a CAN bus, as shown in Figure 46. The main advantage of the active probes' design is that it is a time-optimized system. This design can exclude a switching part from the system, while the receivers should be in the "receiving mode". Subsequently, a multiplexer that would introduce additional delays is neglected. Active measuring probes are divided into digital and analog parts. The digital part is responsible for sending ready measurement results to the tomography controller via the bus. The active probe can work both as a receiver of an ultrasonic signal and as a transmitter. The main controller of the tomograph is responsible for managing the measurement sequence, setting the active probes in the transmit/ receive mode and also saving the results collected from the other probes. The probes are designed so that they can be placed very close to each other. Power lines, communication buses and break lines, which are necessary for the correct implementation of the time measurement from the moment of sending to receiving the signal on other probes, were carried out using RJ-12 cables [1].

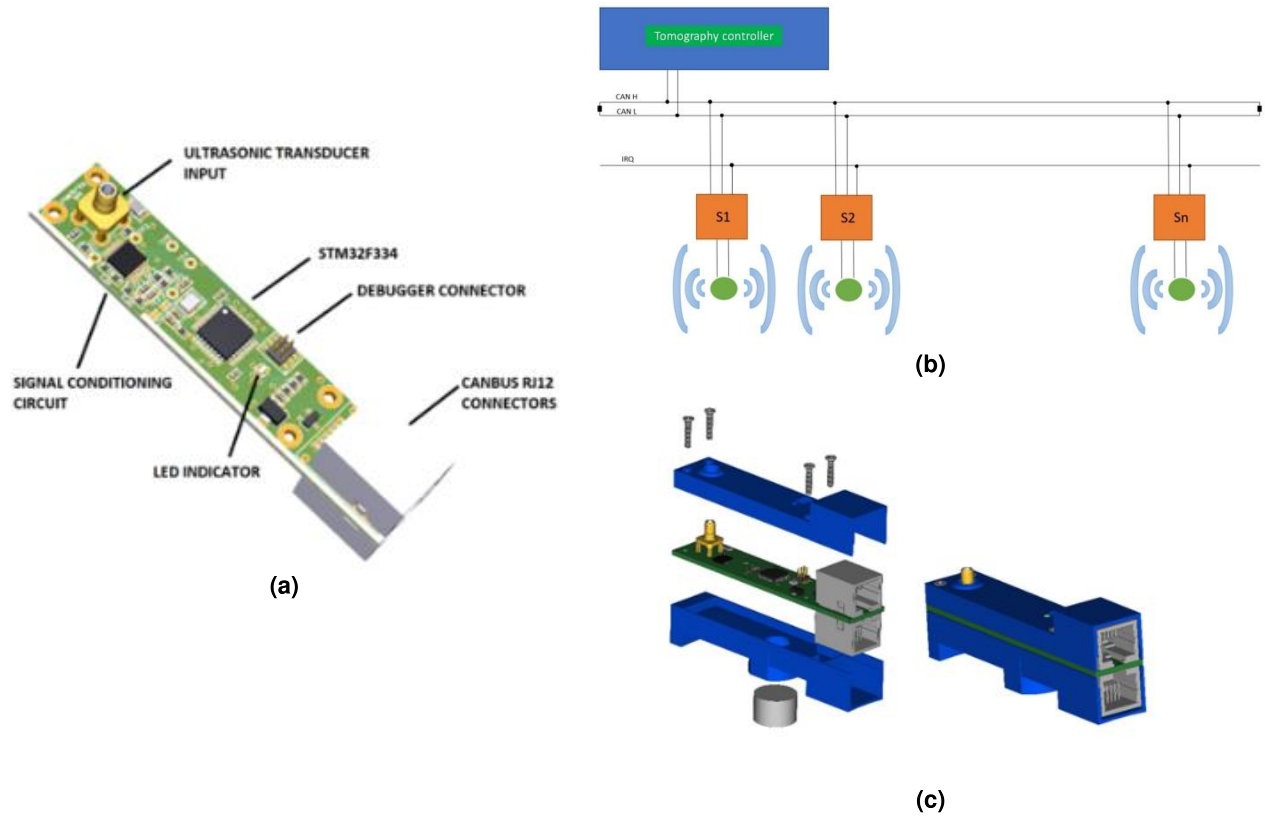

Figure 46: (a) Circuit of the active probe. (b) Block diagram of the ultrasound tomograph. (c) Assembly of the active probe circuit with the sensor.

Figure 47a displays the basic concept of an USCT system for the control of batch crystallisation and generally for stirred tanks environment. The sensors are mounted to the outer surface of the tank using an ultrasonic coupling gel and a belt, keeping the system in place. The sensor array is connected to the main computer unit, processing signal information and providing tomographic evidence, which leads to the characterisation of the process. As shown in Figure 47b, the sensors scan the cross-sectional plane located 5 cm above the bottom of the tank. The measurement device collects data at the arrival time of the first transmitted pulse allowing travel time imaging. Figure 47c presents the first stirred tank, which is made of acrylic material, due to its low acoustic impedance. The thickness of both tanks is about 1 cm. The tank's diameter is 20 cm. The sensors

This project has received funding from the European Union's Horizon 2020 research and innovation programme under the Marie Skłodowska-Curie Grant Agreement No. 764902.

are attached to the outer surface, being non-destructive, and the pulses travel through the wall of the tank. As the sensors are attached in the outer surface of the tank's wall, the reconstruction software accounts for the pulses' penetration of the tank's wall, to better calculate the time-of-flight (TOF) values providing more accurate raw values describing mainly the medium material's characteristics.

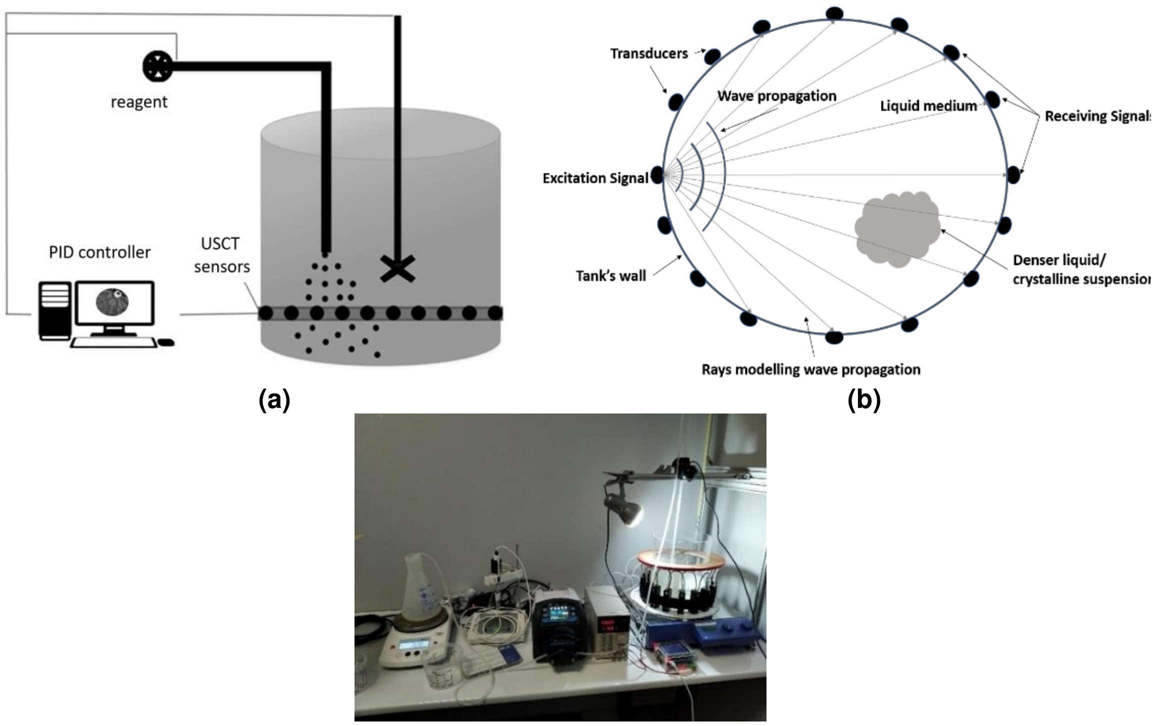

Figure 47: (a) Graph depicting USCT implemented in a batch crystallization set-up. (b) USCT functionality (panoramic view). (c) USCT ring array integrated to a 20 cm diameter acrylic tank.

9.1.2 Measurement data

One of the active probes sends an ultrasonic signal of 5 cycles (tone burst), the rest of the probes are in receiving mode. Active probes measure the time from the moment the signal is sent until it is picked up by individual transducers. This is the time-of-flight of the pulse (TOF). The sequence repeats until each probe produces a signal and all times are collected. Figure 48a shows the signal waveform for one pair of transducers. The signal is fed into a rectangular signal fed to the ultrasound transducer in order to force transmission (probe). The obtained signal is the shape of the signal wave at the transducer output, which is then transformed into a rectangular signal (processed signal) so that it can be read by the digital input of the microcontroller. The red segment is the measured time that is sent to the control unit. Due to the active measuring probes, the analogue signal path has been reduced to a minimum, which reduces the level of interference. The probes communicate with the main unit via the digital CAN bus. The concept of an active probe enables the switching system to be switched off from the rest of the system. Avoiding a multiplexer, which would introduce additional delays, we optimize the time of recording the data.

This project has received funding from the European Union's Horizon 2020 research and innovation programme under the Marie Skłodowska-Curie Grant Agreement No. 764902.

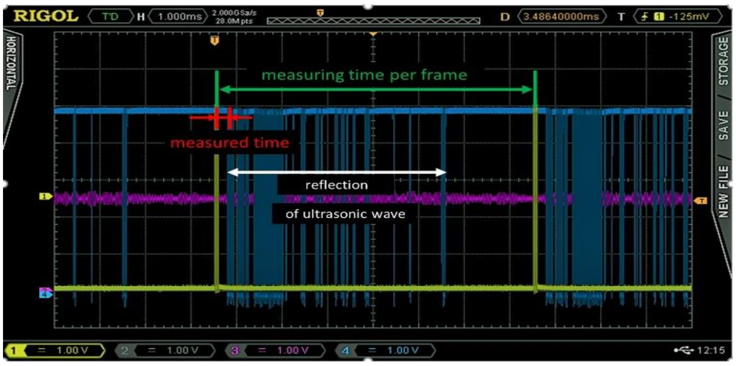

(a)

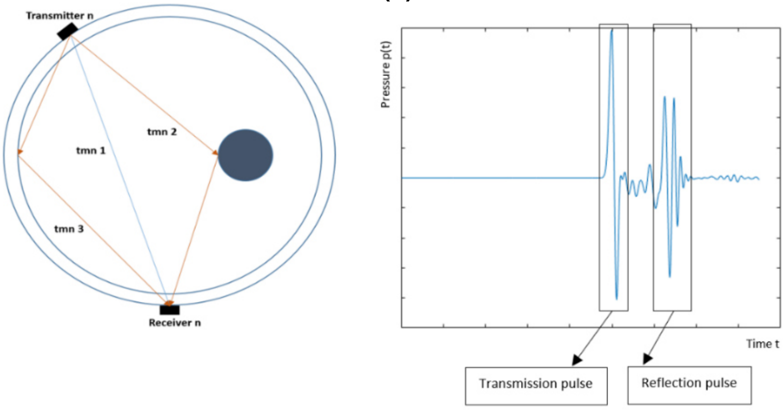

(b)

Figure 48: (a) Display of the transmitted, received and filtered pulse of a single measuring frame. (b) Three possible ways of receiving information by the wave's propagation. The circular perimeter displays the tank and the dark blue circle inside it displays the object. The form of a received signal.

The time of one measuring frame depends on the ultrasonic reflection and backscattering factor inside the tank. Thereafter, the next, consecutive actuation of sensors can be done only after these pulses completely attenuate. Figure 48a shows the recorded reflections and in the same figure, 48b shows the geometric paths of the transmitted and reflected recorded signals. This is a serious problem because these reflections prolong the time of a single measurement for a much longer time than a pulse needs to travel inside the tank (transmission time). For example, the times to be measured are of the order of hundreds of microseconds, while the reflections/backscatters of ultrasonic waves last several milliseconds. Depending on the number of measuring probes, the time required to collect the data needed to create one image will be a multiple of the time of a single measurement and the number of measurement probes. In the case of the test container for 16 measurement probes, obtaining data for one image takes about 120 msec. So, the temporal resolution of the system is about 4 frames per second accounting for the time the reconstruction algorithms need to be performed [2].

9.1.3 Reconstruction method

We developed a transmission tomography framework, for this work. Transmission tomography is based on the transmitted pulses and their characteristics. It can be either a travel-time or sound-speed technique measuring the time of traveling of the first-arrival pulse. The most commonly used

This project has received funding from the European Union's Horizon 2020 research and innovation programme under the Marie Skłodowska-Curie Grant Agreement No. 764902.

approximation for transmission USCT is the ray-based method. It is the fundamental foundation for the most tomographic schemes, as the line integral defines the path of a high frequency propagating pulse between an emitter and a receiver. However, this is a simplified approach which is not accounting for the diffraction effect caused by the inhomogeneousness of the medium. To tackle this, we used a computational model based on diffraction on the 1st Fresnel zone, depicted in Figure 49a.

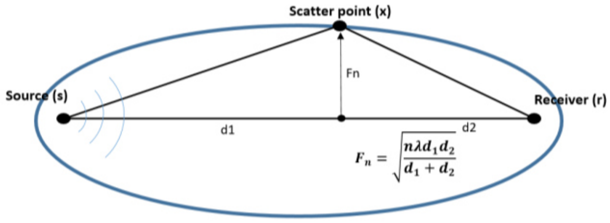

(a)

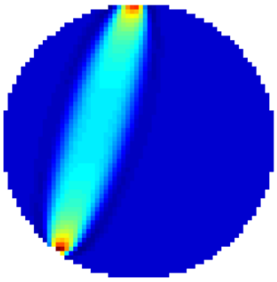

(b)

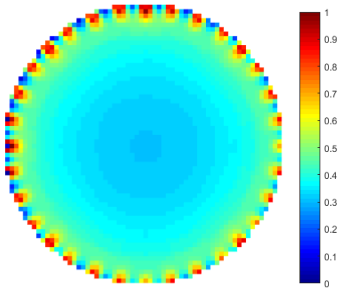

(c)

Figure 49: (a) Fresnel zone geometry including the calculation of the radius. (b) Frechet Sensitivity Kernel with a centre frequency of 40 kHz for one measurement. (c) Overall sensitivity matrix plot (sum of all sensitivities), displaying the sensitivity distribution of the modelled matrix.

Fresnel volume or 'fat ray' tomography is an appealing compromise between the efficient ray theory tomography and the computationally intensive full waveform tomography [3]. Using a finite frequency approximation to the wave equation leads to a sensitivity kernel where the sensitivity of the travel time delay also appears in a zone around the fastest ray path. The delay time is given as:

$$\Delta t(x) = t(s,x) + t(x,r) - t_0(s,r) \tag{24}$$

Here t(s, x) and t(x, r) are the travel time from the source (s) to x and from x to the receiver (r) and $t_0(s,r)$ is the travel time along the ray path from the source to the receiver. One can evaluate the times of traveling using the ray tracing method. A point x is always within the first Fresnel zone if the corresponding travel-time satisfies the following equation, in which T defines the emitted wave's period:

$$|\Delta t(x)| < \frac{T}{4} \tag{25}$$

The following function defines the sensitivity of a Frechet kernel based on the first Fresnel zone:

This project has received funding from the European Union's Horizon 2020 research and innovation programme under the Marie Skłodowska-Curie Grant Agreement No. 764902.

$$S(x) = K\,\mathrm{V}(s,x)\,\mathrm{V}(x,r)\cos\left(2\pi\frac{\Delta t(\chi)}{T}\right) exp(-\left(\frac{a\Delta t(x)}{\frac{T}{4}}\right)^2) \tag{26}$$

Where S(x) is the sensitivity at x, V(x,y) is the amplitude at Y of the wave field propagating from X, and K the normalization constant. The cosine factor models the alternating sensitivity being positive in the odd Fresnel zones and negative in the even Fresnel zones. The a, in the Gaussian factor, controls the degree of cancellation in Fresnel zones beyond the first. The amplitude factors have been approximated by the geometrical spreading in a homogeneous medium. The normalization of the kernels is achieved by ensuring that the integrated sensitivity over the whole medium is equal to the length of the reference ray path. SIPPI matlab software has been used to generate these sensitivity kernels [3]. In this work we used Frechet sensitivity maps, described by Buursnick et al. and produced by SIPPI matlab package [4]. Figure 49b depicts a single sensitivity map, representing the sensitivity of an excitation beam from a transmitter to a receiver, while Figure 49c represents the whole sensitivity of the FOV, dscibed by the sensitivity matrix. The plot of Figure 49b comes from the sum of all the the sensitivity maps. All of these kernels, representing the acoustic distribution of the medium of each sensor's excitation, forms the sensitivity matrix. A Normalization method is adding to the final result of the sensitivity matrix to ensure an accurate time-of-flight (TOF) and acoustic-attenuation (AA) mapping as shown in eq. 27.

$$A_{i,j} = \frac{A1_{i,j}}{\sum_{i_1=1}^{m}\sum_{j_1=j} A1_{i_1,j_1}} \tag{27}$$

Where $A1_{i,j}$ is the sensitivity matrix based on the Frechet method and $A_{i,j}$ is the normalized matrix, which is used for reconstructions, with $\mathrm{i} = [1, \dots \mathrm{m}]$ and $\mathrm{j} = [1, \dots, \mathrm{n}]$.
A tomographic approach needs the transmission sensitivity matrix as it simulates the propagation of the measured energy from the sensors. The so-called forward problem is forming by the multiplication of the sensitivity matrix with the measurement data. The TOF measurement data come from the subtraction of background data from the full data and defines the travel-time delays in μsecs. Only the positive of the subtractive data are accounted for as full data always mean to be bigger than the background.

$$TOF = TOF_{back} - TOF_{full} \text{ where } TOF \begin{cases} 0 & if\ TOF < 0 \\ TOF & if\ TOF > 0 \end{cases} \tag{28}$$

The sound-speed (SS) measurement data are computed by eq. 29, using the time data and knowing the exact distance, one can compute sound-speed data, which represents the average sound velocity of every each one of the wave-rays :

$$SS = \frac{D}{\Delta m} \tag{29}$$

Where D is the distance of the travel-path of each ray, SS is the computed average sound velocity of a ray and Δm is the TOF data. The sound speed of the m_{th} ray, SS, s_m (1<m<M) of an acoustic wave that travels through the path l, between an emitter and a receiver. Below the notation defines ΔM which stands for both TOF and SS data for travel-time and SS imaging. A generalised tomographic forward problem can be expressed as:

This project has received funding from the European Union's Horizon 2020 research and innovation programme under the Marie Skłodowska-Curie Grant Agreement No. 764902.

$$\Delta M = A\,\Delta S + e \tag{30}$$

Where ΔS is the reconstructed distribution based on acoustic features, A is the modelling operator which expresses the sensitivity distribution in the FOV, ΔM is the sensor's recorded data and e is the noise in the measurements. A simplified inversion can be done using back projection.

$$\Delta S \approx A^T \Delta M \tag{31}$$

The total Variation regularization (TV) was used, which has a greater potential in solving the regularized inverse problem in a stabilized fashion. The TV problem is defined as an optimization problem.

$$minA(\Delta S) = ||(A\,\Delta S + e) - \Delta M||^2 + \alpha\, \left||\nabla \Delta M|\right|_1 \tag{32}$$

Where a, the regularization parameter, ∇ is the gradient and $\left||.|\right|_1$ is the l_1−norm. Then the problem to be solved is the constrained optimization problem as shown in equation 33.

$$x_a = arg\,min_{\Delta S}\left(\alpha\left||\nabla \Delta S|\right|_1\right) \text{ such that } \left||A\,\Delta S - \Delta M|\right|^2 < p \tag{33}$$

This is solved by the Split Bregman based TV algorithm [5]. Carefully choosing the regularization parameter, we optimize the image by deleting undesired artefacts.

9.2 Implementation in process

9.2.1 SS quantitative imaging

Experiments were carried out to test the response of the developed sound-speed imaging algorithms which could be a promising tool for characterizing liquid compounds of different densities [6]. Sucrose/water solutions were used in different unsaturated concentrations. Six unsaturated solutions of 20 %, 33 %, 42.86 %, 50 %, 56.52 % and 60.78 % mass/volume concentration (m/vol %) of white granulated sugar (sucrose) and tap water at 20°C were created, while the saturation point of this particular mixture is 66.7 % m/vol. These solutions were used as inclusions in the tank, which was filled with a medium of tap water at 20°C. The receiving tank was filled with tap water in the room's temperature. Figure 50a displays the experimental process. Figure 50b displays the results of a 20 % concentration test, while Figure 50c the 60.78 % concentration test. Figure 50d presents a graph that indicates the sound velocity profile over the liquid's density factor. The concentration points were matched with density values, according to the single-measurement study of the same experimental scenario implemeted by Resa et al [7].

This project has received funding from the European Union's Horizon 2020 research and innovation programme under the Marie Skłodowska-Curie Grant Agreement No. 764902.

(a)

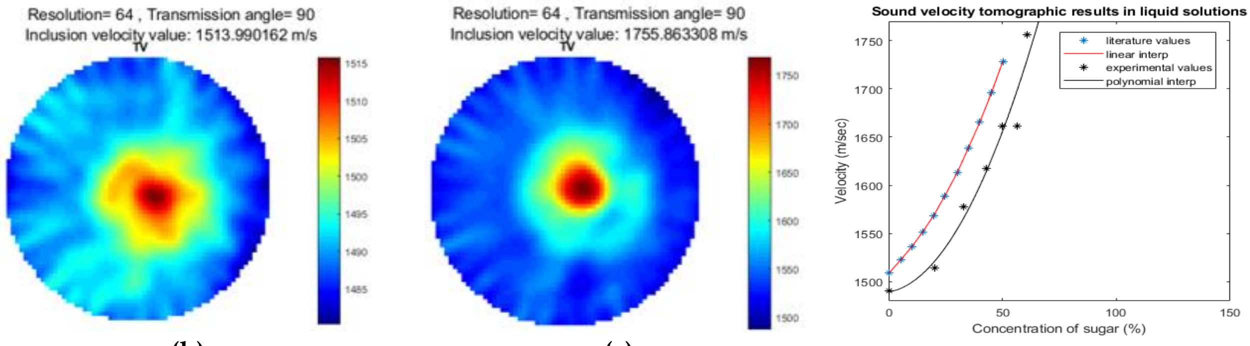

(b) (c) (d)

Figure 50: (a) Experimental set-up. (b), (c) Experiments with 20 % and 60.78 % concentration of sucrose/water mixture. The scale of reconstructions is in sound-speed units (m/s). (d) Graph of concentrations values. Experimental values are represented with black dots and single measurements values form literature studies represented with blue dots. Literature values extracted from Resa et al study [7].

9.2.2 Travel-time imaging for batch crystallization

Figure 51 presents none stirring calcium carbonate crystallisation experiments [8]. The basis of the crystallisation process is the reaction of a sodium carbonate solution (reagent) with a calcium chloride solution. The chemical reaction is described in equation 34.

$$CaCl_2^{aq} + Na_2CO_3^{aq} \rightarrow CaCO_3 + 2NaCl^{aq} \quad (34)$$

Due to the lack of dynamics, immediate crystalline suspensions are formed to the location where the injection point is. Crystallisation is happening regionally and in faster pace. The injection point was being shifted manually. Therefore, the formation of crystalline suspensions follows the movement of injection. For this experiment the 20 cm propylene tank was used. The reagent's feed rate was 20 mL/min. Denser suspensions are immediately created during the injection of the reagent. The denser suspensions start sedimenting. While the suspensions go down, they are passing through the FOV of the sensors. Figures 51a-d show photos from the experiments in different moments. The reconstructed results agree with the shape of the forming crystals, presented in Figure 51e. An interesting point is that regions with a constant injection over a point reach high TOF delays values, and when the injection point moves, the region goes to lower values again. This is due to the immediate crystal formation, especially in this type of reactive crystallisation. However, when the injection point moves, the crystallisation in the region stops and subsequently the already created crystalline suspensions whether start dissolving or start sedimenting. Therefore, one can notice this decay of TOF delays values after the moving of the injection in the reconstructed frames.

This project has received funding from the European Union's Horizon 2020 research and innovation programme under the Marie Skłodowska-Curie Grant Agreement No. 764902.

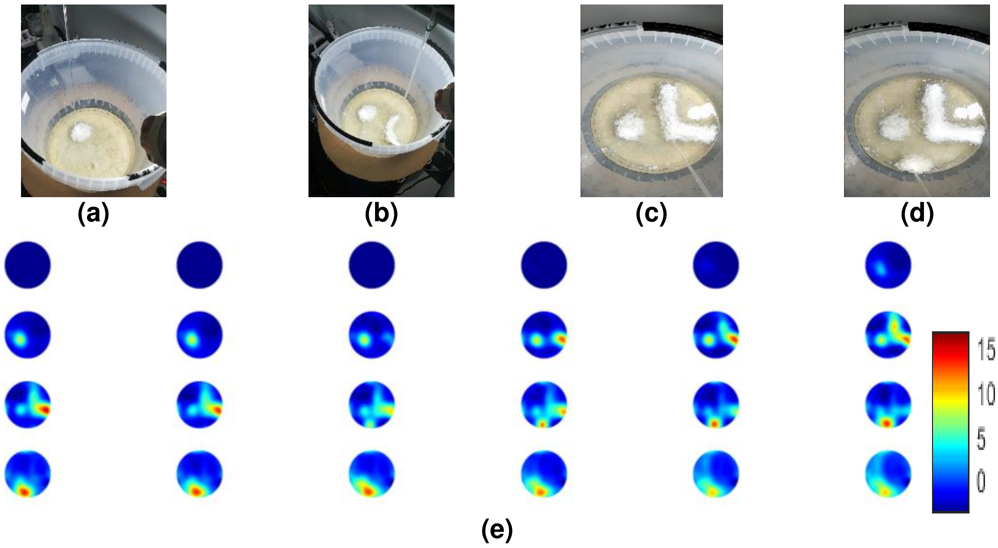

Figure 51: (a)-(d) Photos of the experiment and reconstructions. (e) Reconstruction with the specific capture time.

9.3 Conclusions

The aid of such a USCT device in industrial stirred tanks processes and especially in batch crystallization proved significant. Sound-speed imaging showed good performance providing a clear relation between quantitative imaging and density characterization of liquid solutions for industrial purposes. The developed sound-speed USCT could be of a help in industrial miscible liquids processes by distinguishing for liquid mixing-cases, characterizing uniformity of mixtures, calculating approximate sound-speed distributions and offering density indications of liquid mixtures. Furthermore, the travel-time imaging displayed many useful application in batch crystallization experimental apparatus. Despite the fact that such a device has not the potential of imaging or even measuring the particle's size directly, it seems that it could be of great aid in crystallisation processes as monitoring homogeneity or detecting malfunctions and faults. It could work as a quality assurance figure to protect from significant mistakes that could lead to a rough crystal yield. Using it as a pre-step in a process-control loop to identify malfunctions during the process, could also be a significant advantage to the automatic control of batch crystallisers processes. Important conclusions are the determination of:

- Reaction progress by the mean TOF delays values
- Homogeneity of the medium during injection process by the reconstructions
- Unwanted by-product formation by the reconstructions

A significant amount of crystallization experiments have been done in lab environment and the USCT data has been analysed in many ways to better understand the extends of the developed method. The studies on stirring, injection rate and other parameters, which can affect the outcomes of the process, and subsequently the quality of the yield, will be the continuation of this study.

This project has received funding from the European Union's Horizon 2020 research and innovation programme under the Marie Skłodowska-Curie Grant Agreement No. 764902.

9.4 References for USCT in batch crystallization

[1] T. Rymarczyk, M. Golbek, P. Bozek, P. Adamkiewicz, M. Maj, J. Sikora, The prototype ultrasound tomography device to analyze the properties of processes, *2018 Appl. Electromagn. Mod. Tech. Med. PTZE 2018*, pp. 228–231, 2018.

[2] P. Koulountzios, T. Rymarczyk, M. Soleimani, Ultrasonic Tomography for automated material inspection in liquid masses, *9th World Congr. Ind. Process Tomogr. WCIPT9, Sep. 2018*, pp. 693–702, 2018.

[3] T. Mejer Hansen, K. Skou Cordua, M. Caroline Looms, K. Mosegaard, SIPPI: A Matlab toolbox for sampling the solution to inverse problems with complex prior information: Part 1-Methodology, *Comput. Geosci.*, Vol. 52, pp. 470–480, Mar. 2013.

[4] M. L. Buursink, T. C. Johnson, P. S. Routh, M. D. Knoll, Crosshole radar velocity tomography with finite-frequency Fresnel volume sensitivities, *Geophys. J. Int.*, Vol. 172, No. 1, pp. 1–17, Jan. 2008.

[5] F. Li, J. F. P. J. Abascal, M. Desco, M. Soleimani, Total Variation Regularization with Split Bregman-Based Method in Magnetic Induction Tomography Using Experimental Data, *IEEE Sens. J.*, Vol. 17, No. 4, pp. 976–985, 2017.

[6] P. Koulountzios, T. Rymarczyk, M. Soleimani, A quantitative ultrasonic travel-time tomography to investigate liquid elaborations in industrial processes, *Sensors (Switzerland)*, Vol. 19, No. 23, 2019.

[7] P. Resa, L. Elvira, F. Montero De Espinosa, Y. Gómez-Ullate, Ultrasonic velocity in water-ethanol-sucrose mixtures during alcoholic fermentation, *Ultrasonics*, Vol. 43, No. 4, pp. 247–252, 2005.

[8] P. Koulountzios, T. Rymarczyk, M. Soleimani, Ultrasonic time-of-flight computed tomography for investigation of batch crystallisation processes, *Sensors (Switzerland)*, Vol. 21, No. 2, 2021.

This project has received funding from the European Union's Horizon 2020 research and innovation programme under the Marie Skłodowska-Curie Grant Agreement No. 764902.

10 Electrical resistance tomography and quantitative evaluations in crystallization

The monitoring and control of the crystallization processes are inherently challenging due to the different types of crystallization techniques involved such as cooling crystallization, anti-solvent crystallization, and reactive crystallization. Each of these types requires a different kind of process analytical tool or method for the process progress evaluation. Advances have been made in the modeling, monitoring, and control of the crystals and one-dimensional PAT evaluations involving combined cooling and antisolvent crystallization by measuring temperatures and analyzing microscopic images of crystals along with the observation of kinetics [1–3]. Electrical resistance tomography (ERT) is one of the novel process analytical tools used to monitor the crystallization process. The 2D ERT allows us to detect and visualize the conductivity distribution inside the chemical reactor using electrical voltage or current measurements acquired from the periphery of the reactor. This is utilized to evaluate the different stages of the process [4].

To produce value-added products in chemical industries, PAT is particularly utilized in large-scale reactors and tanks. The large-scale chemical process industries have used the ERT extensively to monitor the unbaffled stirred tanks and reactors to check the solid and liquid distribution [5]. A multi-layered ERT system has been used to visualize the dense solid particles in a solid-liquid stirred tank and observe precipitation reactions [5, 6]. Large-scale crystallization monitoring and control and to improve predictability and robustness of the chemical reaction products can also be performed using ERT.

The quantitative accuracy of the ERT evaluations depends on various factors as mentioned in Figure 52. It can be broadly classified into factors arising due to the electronic hardware utilized and the physical/chemical composition of the solution/mixture under study. It also depends, in the case of crystallization, on the type of crystallization method used. The differences in the conductivity profile of the materials under consideration play a very important role in the detection of the target object. The computational and image processing algorithms used also play a major role in determining the quantitative analysis of the crystal within the region of interest of the reactor. Some of the factors are the FEM mesh model structure chosen, the fine FEM meshes would provide better resolution but would increase the computation times. The reconstruction algorithm and the number of iterations of the reconstruction method affect the accuracy of measurements. Along with image segmentation or the thresholding method and morphological image processing algorithms, the calibration of the 2D-ERT images must be performed in order to obtain the highest possible quantitative accuracy. Apart from this, the other factors which affect the quantitative estimation are the location of the object inside of the reactor (near the sensor provides higher accuracy) and the number of objects inside the solution.

These factors were tested in [7] to arrive at the standard calibration for quantitative evaluation of the crystal flow for the dynamic experiments presented in chapter 3.

This project has received funding from the European Union's Horizon 2020 research and innovation programme under the Marie Skłodowska-Curie Grant Agreement No. 764902.

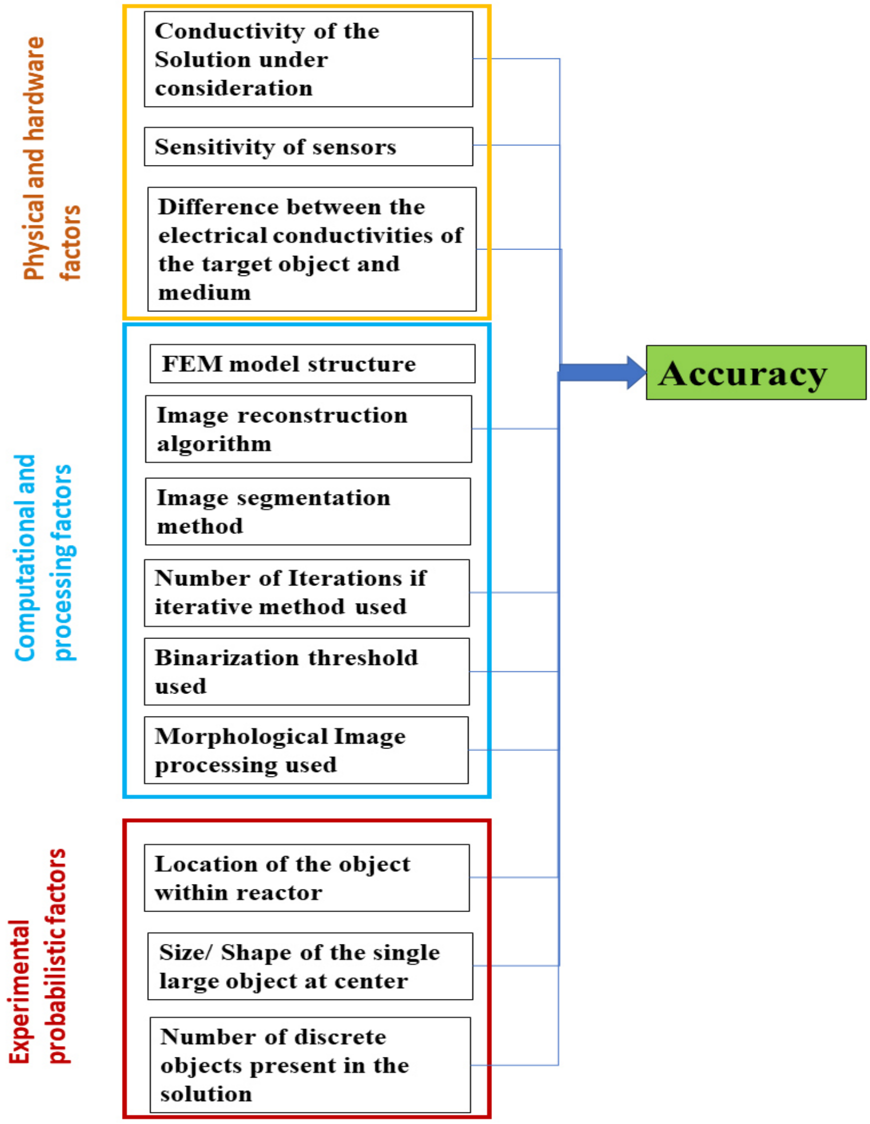

Figure 52: Factors influencing the accuracy of the image object in the ERT reconstructed image.

10.1 Sensor hardware design and experimental construction

10.1.1 ERT sensor and measurement electronics

The ERT measurement system consists of metal electrodes surrounding the sensing region of interest within the reactor. The general data acquisition and data processing units are shown in Figure 53. This consists of the integrated signal conditioning and processing unit which was specifically designed for the measurement in the low conductivity environment. The Voltage injected Current detected type -ERT from Rocsole Ltd was used in the experiments. The system was connected to 16 stainless steel electrodes placed on the circumference of a single measurement plane. The outer diameter of the semi batch reactor measured 90 mm. The electrodes were screws of 12 mm diameter head facing region of interest made of stainless steel. The electrodes were installed in the pipelines via drilled holes. A sealed using rubber sealing of 2 mm thickness was added in the inner side of the pipeline. This setup is shown in Figure 54a-c. Inhouse developed software TomoKis [8]

This project has received funding from the European Union's Horizon 2020 research and innovation programme under the Marie Skłodowska-Curie Grant Agreement No. 764902.

studio was used for live image reconstruction and data acquisition. All the 256 measurements of each frame are saved by the sensor, at a frequency of 14 Hz. In order to match the impedance range of the signal with the target media, the electrodes were connected to the electronics using a signal conditioning unit. Coaxial cables type RG178 of length 2.5 m were used for the connection between measurement electronics and the signal conditioning unit as well as from the signal conditioning unit to the sensor.

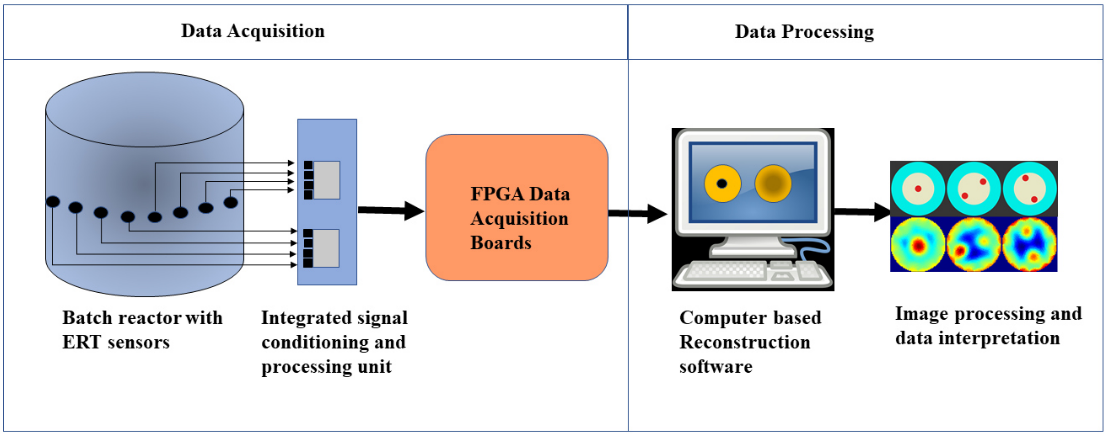

Figure 53: Schematic of the ERT data acquisition and data processing system.

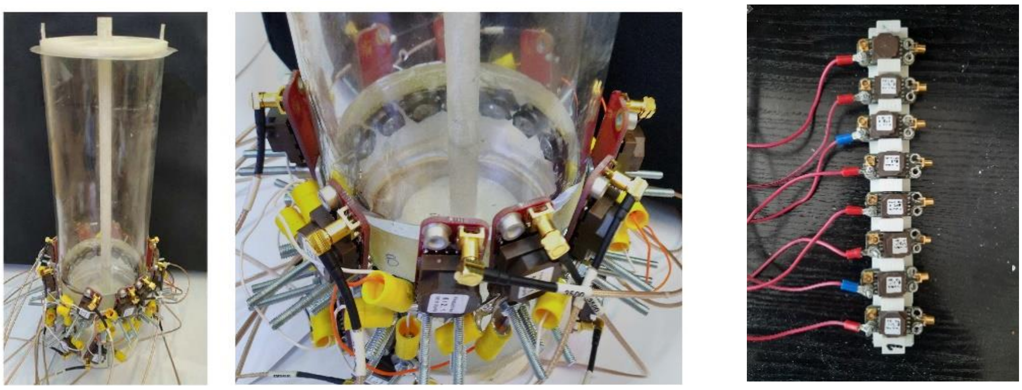

(a) (b) (c)

Figure 54: (a-b) Setup of the laboratory-based batch reactor with sensor and signal conditioning unit mounted on the reactor (c) signal conditioning unit mounted on the 3D printed frame.

10.1.2 Phantoms and sensor calibration

Five cylindrical 3D printed ABS phantoms were 3D printed for the static measurements, with diameters of 50 mm (R1), 40 mm (R2), 30 mm (R3), 20 mm (R4), 10 mm (R5). Along with this, there was an additional phantom with 2 x 10 mm diameter (R6). These phantoms are shown in Figure 55a-c. The phantoms were relatively heavy as compared to the PLA phantoms used previously. They were stable in the liquid and did not fall due to the buoyant force exerted by the liquids. Figure 55a shows the 3D phantoms designed using Blender v 2.79 software.

This project has received funding from the European Union's Horizon 2020 research and innovation programme under the Marie Skłodowska-Curie Grant Agreement No. 764902.

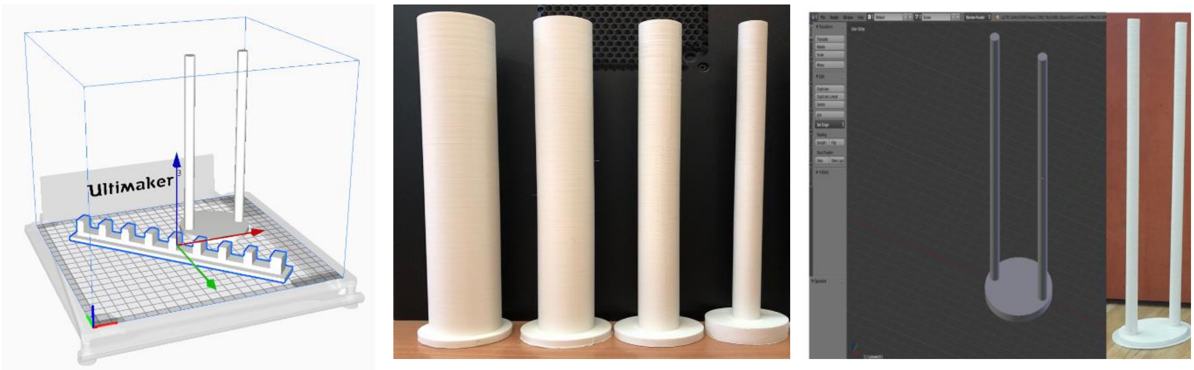

Figure 55: (a) 3D design (b) ABS phantom (c) Phantom R6.

10.2 Data processing results

10.2.1 Comparison for Phantom R6

In Figure 56, reconstructions of phantom R5 and R6 at locations L1 and L2 can be seen qualitatively. In Figure 56a, the differences between the reconstructions for tap water are visible for phantoms R6. In Figure 56b for industrial-grade saturated sucrose solution, the objects are separated only in total variation segmentation. Other methods give background noises. The LBP method in Figure 56c fails to detect and separate phantoms in demineralized water. The phantoms are separable and visible with the total variation method.

This project has received funding from the European Union's Horizon 2020 research and innovation programme under the Marie Skłodowska-Curie Grant Agreement No. 764902.

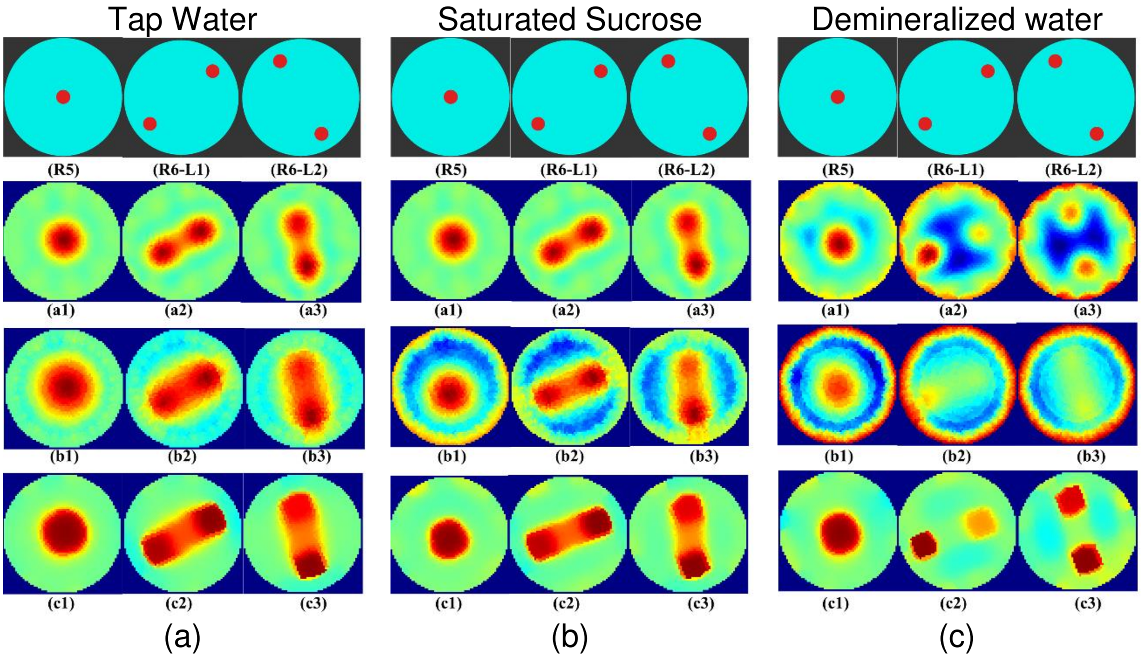

Figure 56: (a) Tap water. (b) Industrial grade saturated sucrose solution. (c) Demineralized water: (R5, R6-L1, R6-L2) Phantom reference (a1-a3) Gauss Newton reconstructions (b1-b3) LBP reconstructions (c1-c3) TV reconstructions at 10 iterations.

10.2.2 Comparison to reference after G-Channel segmentation

The extracted RGB color channels for phantom R6-L1 (location 1) in demineralized water are shown in Figure 57b-d. They were obtained by using the MATLAB image processing toolbox functions otsuthresh(), adaptthresh(), and imsegkmeans(). The local adaptive threshold creates multiple non-connected regions in the image. This would require additional processing methods. Also, image segmentation using Otsu, local-adaptive threshold, and the K-means method with three regions for Phantom R6-L1 can be seen in Figure 57f-h. Otsu segmentation fails to detect the second phantom. With G-Channel segmentation, both the phantoms are visible with the binarization threshold set at 0.6. The binarization threshold can be varied from 0.1 to 0.9 and is used after extracting the green color channel (G-Channel) image.

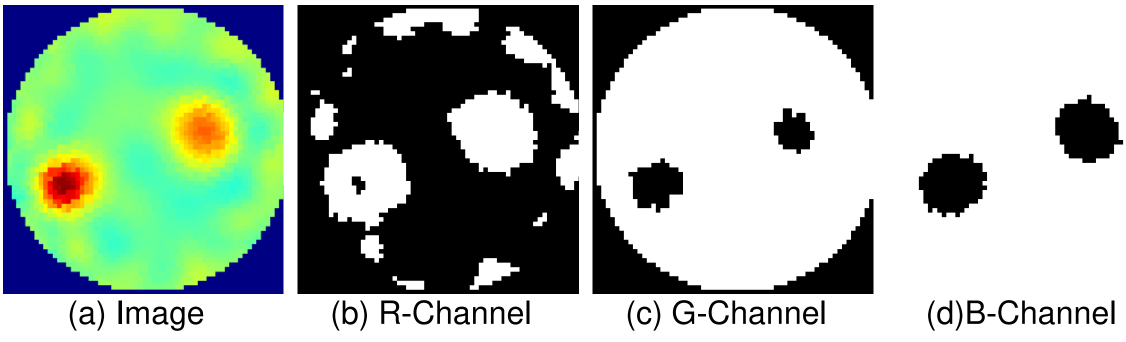

This project has received funding from the European Union's Horizon 2020 research and innovation programme under the Marie Skłodowska-Curie Grant Agreement No. 764902.

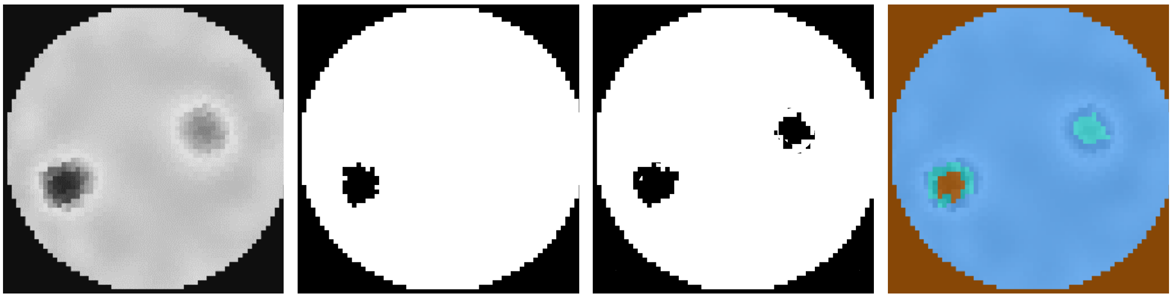

(e) grey (f) Otsu (g) Local-adaptive (h) K-means

Figure 57: Various image segmentation methods for Phantom R5. Solution: Demineralized water, Reconstruction method: Total Variation, Iterations: 2.

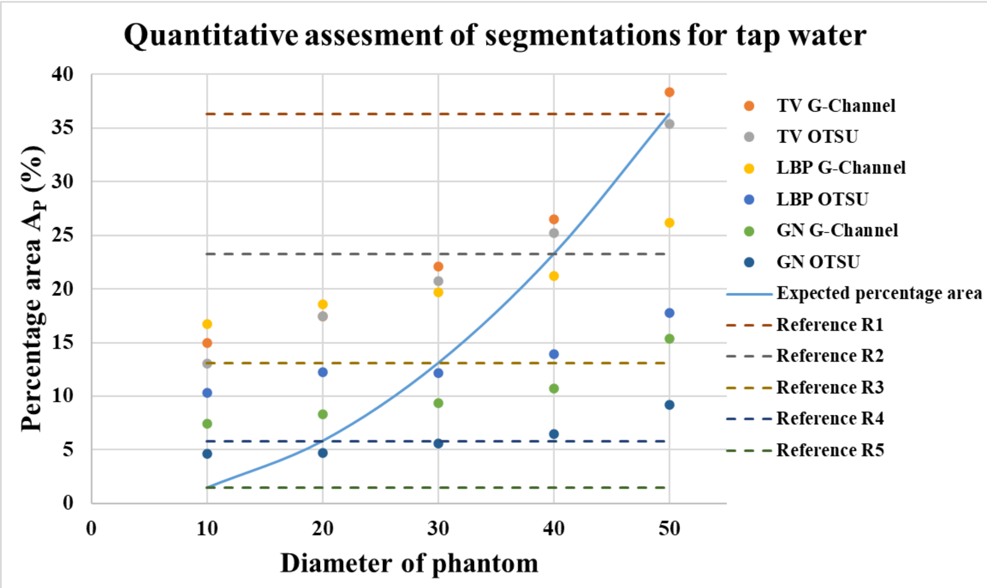

Figure 58: Comparison of the area percentage for Otsu and G-Channel segmentation using TV, LBP, and GN reconstructions for (a) R1, (b) R2, (c) R3, (d) R4, and (e) R5.

Figure 58 shows the results obtained for tap water for various reconstruction methods and segmentation methods and compares it to the standard 3 printed reference for the Phantoms R1 to R5.

10.2.3 Contrast profile assessments

The influence of the change in iterations using contrast profile plots for phantoms R1 to R5 on the G-Channel segmentation is shown in Figure 59. The variation in iterations for the phantoms R6 using contrast profile plot for the G-Channel segmented with threshold 0.6 is also shown in this figure. The contrast profile plots are compared to the reference images. It can be observed that lower iterations give results near to the actual width of the reference phantoms.

This project has received funding from the European Union's Horizon 2020 research and innovation programme under the Marie Skłodowska-Curie Grant Agreement No. 764902.

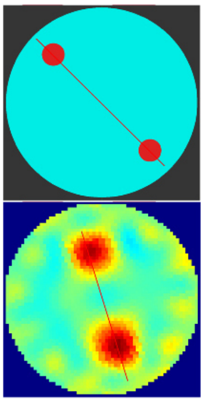

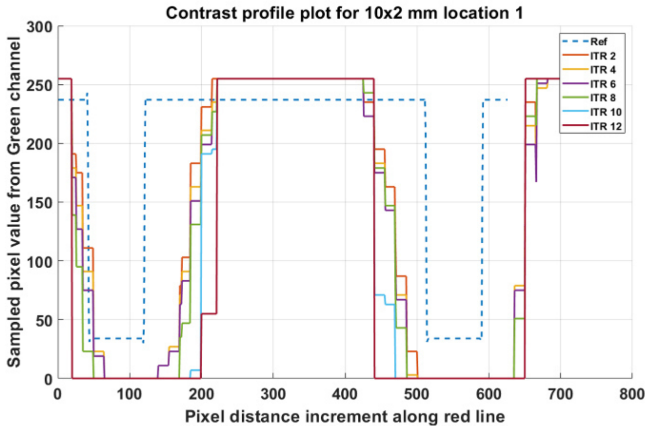

Figure 59: Contrast profile plot for Phantom R6-L2 (2 x 10 mm), Reconstruction: TV, Iterations: 2-12; Channel: Green, Location: 2.

This project has received funding from the European Union's Horizon 2020 research and innovation programme under the Marie Skłodowska-Curie Grant Agreement No. 764902.

10.3 Implementation in process space using dynamic crystal flow: Experimental and performance analyses

Method	Frame 188	Frame 347	Frame 531	Frame 559
	No sugar	Crystal flow	Crysltal flow	Crystal flow
Total Variation	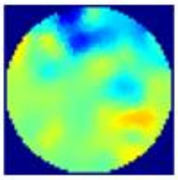	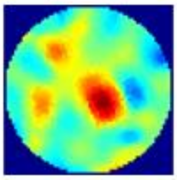	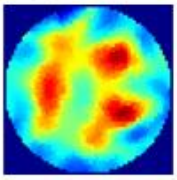	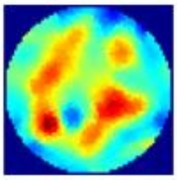
Grey Image	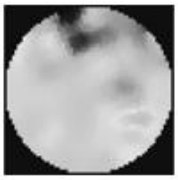	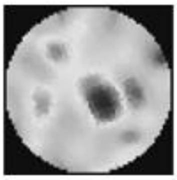		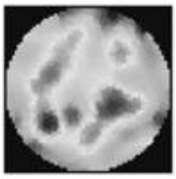
G-Channel segmentation at 0.6				
Otsu segmentation		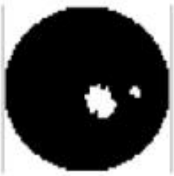		
Area G-Channel Ac (%)	4.48	5.44	11.24	8.81
Area Otsu Ac (%)	3.44	2.70	4.34	4.34

Figure 60: Visualization of the sugar crystals in the demineralized solution at various frames representing time points. Reconstruction: TV, Segmentation: Otsu and G-Channel at threshold 0.6.

The practical applications of the reconstructions and the implementation in the process space to the real experiment involving the insertion of sugar in the demineralized water and visualization using a TV reconstruction algorithm are presented in Figure 60. The sugar crystals weighing 250 g were inserted using a funnel into the experimental batch reactor in the central region. The measurements were acquired at the frame rate of 14 Hz. At frame 188, the insertion of sugar was initiated. Figure 60 presents the reconstructed images of the sugar crystals in the demineralized water. The differences in the conductivities are detected. We can see that apparent differences exist in the conductivity profiles.

This project has received funding from the European Union's Horizon 2020 research and innovation programme under the Marie Skłodowska-Curie Grant Agreement No. 764902.

10.4 Conclusion and ongoing developments

In this work, it was demonstrated that the ERT can be used in the low conductivity solutions such as demineralized water. The practical process space application for sucrose crystals was also tested in the dynamic flow process analysis. The total variation reconstruction algorithm can be used with 2 iterations to evaluate a central object in the reactor with an 83 mm diameter covering an area of 1.5 % of the reactor area in a static testing environment. The expected accuracy was achieved using the G-Channel segmentations on the reconstructed images. The separability of two objects with a 1.5 % area of reactor area was achieved in the demineralized water.

Multiple factors have to be accounted for a quantitative estimation using ERT imaging modality. The discontinuities in the region of interest due to the crystal presence were clearly observed during dynamic testing. It was observed that the total variation algorithm provided good results with G-Channel segmentation as compared to Otsu segmentation for dynamic evaluations.

For quick visualization and analysis of the results of such nature a combined software package is under development. The graphical user interface is shown in Figure 61a and Figure 61b for the software. This software is intended to be used during the calcium carbonate precipitation crystallization experiments planned for the demonstration at Lappeenranta University of Technology. Due to the restrictions in the travel within the European Union to Finland, the experiments have been postponed for a later date until further notice.

This project has received funding from the European Union's Horizon 2020 research and innovation programme under the Marie Skłodowska-Curie Grant Agreement No. 764902.

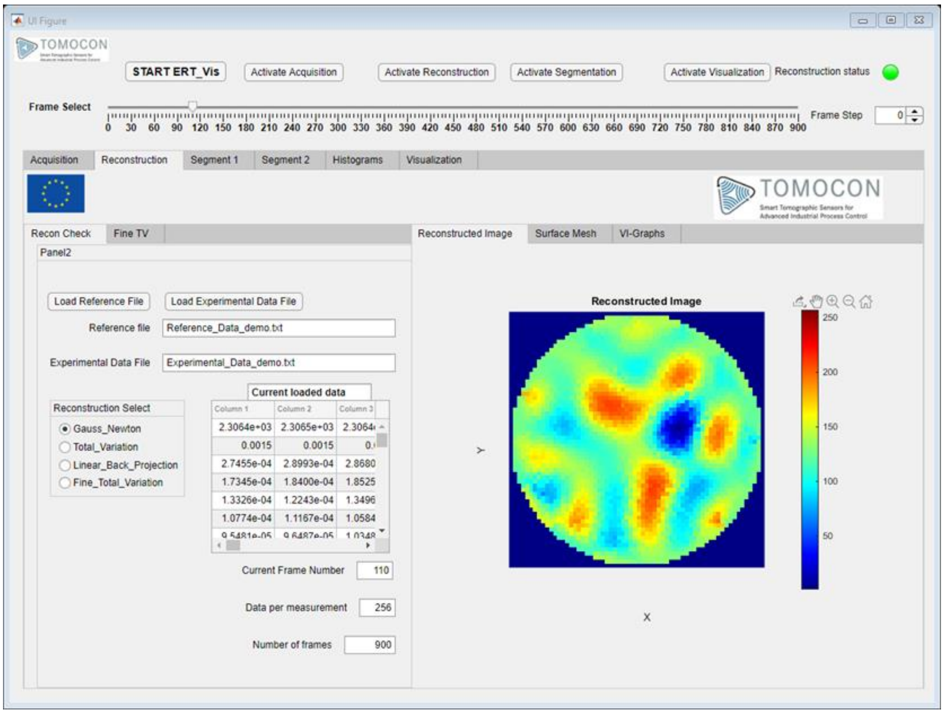

(a)

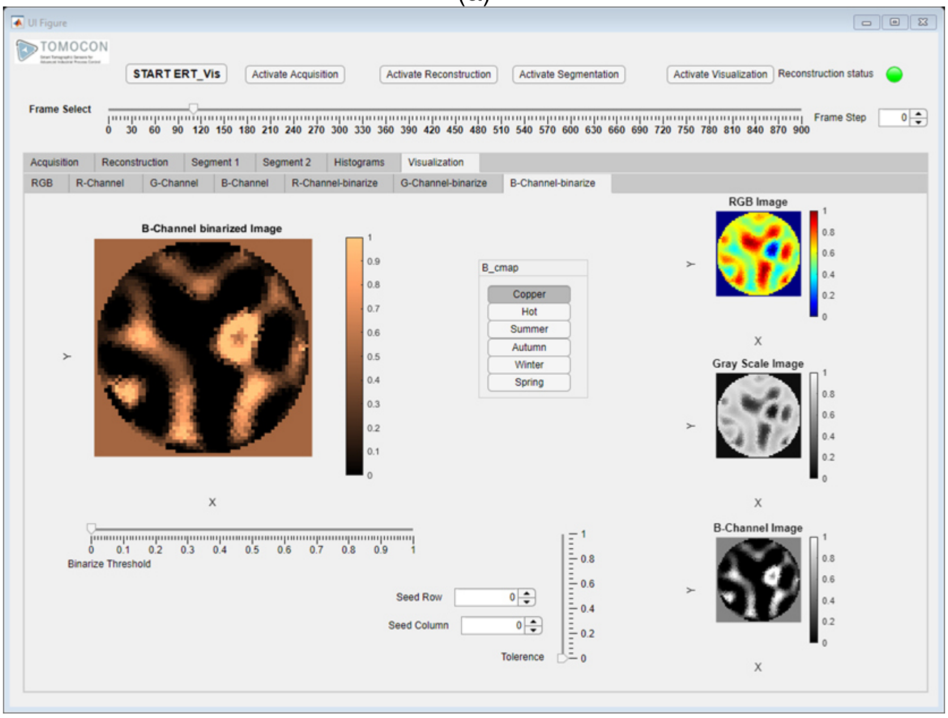

(b)

Figure 61: (a) GUI interface of the reconstruction module of the software. (b) GUI interface for the visualization module of the software.

This project has received funding from the European Union's Horizon 2020 research and innovation programme under the Marie Skłodowska-Curie Grant Agreement No. 764902.

10.5 References for ERT in batch crystallization

1. Z. K. Nagy, G. Fevotte, H. Kramer, L. L. Simon, Recent advances in the monitoring, modelling and control of crystallization systems, *Chemical Engineering Research and Design*, 91, pp. 1903–1922, 2013.
2. C. Lindenberg, M. Krättli, J. Cornel, M. Mazzotti, J. Brozio, Design and optimization of a combined cooling/antisolvent crystallization process, *Crystal Growth and Design*, Vol. 9, pp. 1124–1136, 2009.
3. I. Kovács, P. Harmat, A. Sulyok, G. Radnóczi, Investigation of the kinetics of crystallisation of Al/a-Ge bilayer by electrical conductivity measurement, *Thin solid films*, 317, pp. 34–38, 1998.
4. G. Rao, L. Jackowska-Strumiłło, M. A. Sattar, R. Wajman, Application of the 2D-ERT to evaluate phantom circumscribed regions in various sucrose solution concentrations, *International Interdisciplinary PhD Workshop (IIPhDW),* 2019.
5. C. Carletti, G. Montante, T. Westerlund, A. Paglianti, Analysis of solid concentration distribution in dense solid-liquid stirred tanks by electrical resistance tomography, *Chemical Engineering Science,* 119, pp. 53–64, 2014.
6. S. Stanley, R. Mann, K. Primrose, Interrogation of a precipitation reaction by electrical resistance tomography (ERT), *AIChE journal,* 51, pp. 607–614, 2005.
7. G. Rao, M. A. Sattar, R. Wajman, L. Jackowska-Strumiłło, Quantitative Evaluations with 2d Electrical Resistance Tomography in the Low-Conductivity Solutions Using 3d-Printed Phantoms and Sucrose Crystal Agglomerate Assessments, *Sensors*, Vol. 21, No. 2, p. 564, 2021.
8. R. Banasiak, R. Wajman, T. Jaworski, P. Fiderek, P. Kapusta, D. Sankowski, Two-Phase Flow Regime Three-Dimensonal Visualization Using Electrical Capacitance Tomography – Algorithms and Software, *Informatics Control Meas. Econ. Environ. Prot.*, Vol. 7, No. 1, pp. 11–16, 2017.

This project has received funding from the European Union's Horizon 2020 research and innovation programme under the Marie Skłodowska-Curie Grant Agreement No. 764902.